Urban Climate 67 (2026) 102916

Contents lists available at ScienceDirect

Urban Climate

journal homepage: www.elsevier.com/locate/uclim

Flow and dispersion over a cluster of 'real-world' tall buildings

Changchang Wang [a], Abhishek Mishra [b], Dominic Clements [a], Dianfang Bi [b], Marco Placidi [b], Davide Lasagna [a], Omduth Coceal [c], Janet Barlow [c], Matteo Carpentieri [b], Sue Grimmond [c], Alan Robins [b], Zheng-Tong Xie [a,*]

[a] Department of Aeronautics and Astronatics, University of Southampton, Southampton, SO17 1BJ, UK
[b] EnFlo Laboratory, School of Mechanical Engineering Sciences, University of Surrey, Guildford, GU2 7XH, UK
[c] Department of Meteorology, University of Reading, Reading, G6 6ET, UK

ARTICLE INFO

Keywords:
Urban boundary layer
Cluster porosity
Integral time scale
Dispersive stress
Strouhal number
Gaussian wake deficit
Gaussian plume

ABSTRACT

We focus on a cluster of tall buildings in the City of London, situated within a compact area approximately 700 m in diameter. We uniquely bring together three methodologies to address the impact of densely packed tall buildings on flow and dispersion. We use real-world wind sonic anemometer observations (191 m above ground level) to identify a day with nearly neutral, stationary urban boundary layer flow and determine the integral time and length scales. We use these conditions to inform wind tunnel experiments (1:500 scale) and full-scale high-fidelity large-eddy simulations (LES) with the corresponding integral time and length scales approximated and synthetic inflow turbulence generation applied in the LES. We examine the impact on the building cluster wake region and dispersion of a ground-level release by considering multiple wind directions, and use the wind tunnel-scale observations to evaluate the LES. There is good agreement, with Reynolds number independence of the flow characteristics confirmed under the investigated conditions. The 17 tall buildings exhibit a cluster effect (i.e. acting with unitary effect) on the flow and a ground-level tracer release plume as they pass through the buildings. Despite the cluster porosity having large variations with wind direction, the cluster-area-averaged turbulent stresses are much less sensitive to wind direction than the dispersive stresses. For the least porous direction (SW), the Strouhal number based on the identified primary vortex shedding frequency, freestream velocity and effective cluster width corrected for porosity, is found to be close to that of an isolated tall building. In the far wake, the wake width increases following an approximate power-law trend with an exponent of 0.5, while the peak velocity deficit decreases according to a power-law with an exponent of about −1.0. The peak velocity deficit remains above 10% of the freestream velocity even at approximately 3 km downstream of the building cluster. The tracer plume width increases more rapidly than a linear trend in both horizontal and vertical directions just upwind of the cluster, but downstream its growth follows a power-law trend with an exponent of approximately 0.5. This novel combination of methodologies in the challenging environment of tall buildings offers important insights for a wide range of applications across multiple scales. These findings are becoming increasingly important as urban populations grow and densification trends drive cities to expand vertically.

* Corresponding author.
E-mail address: z.xie@soton.ac.uk (Z.-T. Xie).

https://doi.org/10.1016/j.uclim.2026.102916
Received 28 July 2025; Received in revised form 11 March 2026; Accepted 24 April 2026
Available online 30 April 2026

Nomenclature

b	Average building width
c	Instantaneous concentration
C, C^*	Dimensional and dimensionless mean concentration
C_m, C_m^*	Dimensional and dimensionless maximum local mean concentration at a streamwise distance
d	Roughness displacement height
E	Power spectrum
f, f_p	Frequency and peak frequency
n_p	Nondimensional peak frequency based on wall-normal distance
H	Tallest building height
H_{ave}	Average building height
L	Monin–Obukhov length
L_x, L_y, L_z	Streamwise, spanwise, vertical integral lengths
Q	Emission flow rate
Re_b	Laboratory-scale Reynolds number based on average building width
Re_δ	Laboratory-scale Reynolds number based on boundary layer thickness
$St,\ \tilde{f}$	Strouhal number for dominant vortex frequency and nondimensional frequency based on W_e
T_{int}	Integral time scale
$u, v, w\ (u_1, u_2, u_3)$	Instantaneous streamwise, spanwise, vertical velocities
U, V, W	Mean streamwise, spanwise, vertical velocities
U_0	Undisturbed streamwise velocity at $z = 0.5H_{ave}$
U_d	Wake streamwise-velocity deficit
$U_{d,m}$	Peak wake velocity deficit
$\langle U\rangle, \langle V\rangle, \langle W\rangle$	Horizontally averaged mean streamwise, spanwise, vertical velocities
U_∞	Boundary-top freestream velocity
$\tilde{u}, \tilde{v}, \tilde{w}\ (\tilde{u_1}, \tilde{u_2}, \tilde{u_3})$	Mean streamwise, spanwise, vertical velocity spatial fluctuations
$\langle\tilde{u}\tilde{u}\rangle, \langle\tilde{v}\tilde{v}\rangle, \langle\tilde{w}\tilde{w}\rangle$	Dispersive normal stresses
$\langle\tilde{u}\tilde{w}\rangle$	Dispersive shear stress
$u', v', w'\ (u_1', u_2', u_3')$	Resolved streamwise, spanwise, vertical velocity fluctuations
$\overline{uu}, \overline{vv}, \overline{ww}$	Turbulent normal stresses
$\overline{uw}$	Turbulent shear stress
W_A	Building cluster width (700 m in full scale)
W_e	Effective building cluster width
x_g, y_g, z_g	Geolocated west-east, south-north, vertical coordinates
$x, y, z\ (x_1, x_2, x_3)$	Wind-tunnel streamwise, spanwise, vertical coordinates
x_s, y_s, z_s	Coordinate origin placed at the source location, $x_s = x + 1.25W_A$, $y_s = y, z_s = z$
α	Wind direction
β	Plume centre spanwise coordinate
$\overline{\Phi}$	Time-averaged wavelet magnitude
λ_p	Packing density
λ_f	Frontal area index
λ_s	Building cluster solidity
$\overline{\lambda_s}$	Average cluster solidity
σ_{u_m}	Horizontal-velocity deviation
σ_{ud}	Wake horizontal width
σ_y, σ_z	Plume horizontal, vertical widths
σ_α	Wind-direction deviation from 30-min mean

1. Introduction

By 2050 our cities will host 68% (DESA, 2018) of the world's population, compared to the current 54%, and 33% in the 1960s (UN, 2014). This urbanisation process is often accomplished by the proliferation of tall buildings (TBs) that maximise the provision of housing and commerce using a limited street-level footprint. Tall buildings will, therefore, be even more common in the future, and these can affect local micro-scale climate, pedestrian comfort, and urban air quality. However, a modelling framework accounting for tall building clusters and their wakes is needed, such as for Numerical Weather Prediction (NWP) of wind and dispersion fields. Understanding, modelling, and predicting these wake effects can be of importance to assist and inform policymakers and regulators in building more resilient urban environments, which were the planned aims in the EPSRC funded project 'Fluid dynamics of Urban Tall-building clUsters for Resilient built Environments (FUTURE)'.

Tall buildings are now ubiquitous in many large cities across the globe (e.g. Makedonas et al., 2021). Herein, we refer to tall buildings as structures with a building height to width ratio (aspect ratio, AR) between 3 and 8, and typical heights between 100 m and 300 m (Council on Tall Buildings and Urban Habitat, 2019). Hertwig et al. (2019) show that the wind field downwind of a single 100 m tall building is modified by over 10% for about 500 m (length) and 300 m (width). As the wake region turbulence impact is even more significant, this likely influences pollutant dispersion (Goulart et al., 2019).

Given flow around a single square or rectangular cylinder is a classic bluff body problem, it has received extensive attention (e.g. Bearman and Obasaju, 1982; Lyn and Rodi, 1994; Breuer et al., 2000; Minguez et al., 2011; Trias et al., 2015; Chen et al., 2020). For wind loading the standardised Commonwealth Advisory Aeronautical Research Council tall building model (e.g. Braun and Awruch, 2009; Elshaer et al., 2016) is used as a wind engineering case study.

However, more challenging is understanding the effect of tall structures when closely packed (i.e. a 'cluster' of tall buildings), as typical of high-density and high-rise districts. Large-eddy simulations (LES) (Nguyen et al., 2023) of a two-dimensional cluster (i.e. infinite in spanwise/crosswind direction) with 2×2 square cylinders show that interaction between cylinders influences the aerodynamics performance, with the characteristic length and time scales of the wake associated with the overall cluster size, rather than the individual cylinder geometry, generating a 'cluster effect'. Wind tunnel experiments (Mishra et al., 2023) of idealised tall building clusters with different aspect ratios identify three wake regimes (near-, transition-, and far-wake) with distinct characteristics and scaling laws based on the overall array width. This wake analysis when extended to turbulent fields (Mishra et al., 2024), suggests multi-scale vortex-shedding frequencies exist downwind of tall building clusters, which are influenced by both geometric characteristics of the individual buildings comprising the cluster, and the latter as a whole. Both experimental and LES studies (Mishra et al., 2023, 2024; Nguyen et al., 2023; Inam et al., 2026) confirm that the smaller wakes generated from individual buildings eventually merge into a single, larger wake structure. Mishra et al. (2023) noted that, provided one goes sufficiently downstream of a building cluster (in the far regime as defined in Mishra et al. (2023)), the individual building wakes merge, and an overall cluster wake scaling with the width of the cluster emerges. As a consequence, a single dominant shedding frequency emerges.

Field measurements of wakes from tall buildings embedded within urban canopies are challenging because of sensor mounting. Mast-based (e.g. sonic anemometers) and ground-based sensors (e.g. Doppler Wind Lidar, DWL) have complementary constraints. DWL sensors allow urban boundary layer wind fields to be measured to greater heights than sensors installed on masts (e.g., Allwine et al., 2002; Barlow et al., 2011; Drew et al., 2013; Filioglou et al., 2022; Morrison et al., 2025). Theeuwes et al. (2025) use a DWL to measure the wakes from a single tall building for a site in London where wind tunnel observations have been undertaken (Hertwig et al., 2019). They observed that wake lengths were typically 120–300 m long, and were 80–150 m wide. These sizes were, however, subject to atmospheric conditions, with unstable boundary layers producing shorter and narrower wakes, while stable conditions resulted in less significant differences. It was also observed that higher upstream roughness reduced stability effects. DWLs observations of bridge and wind turbine wakes (Nafisifard et al., 2023; Sun et al., 2020) may also be informative to understanding urban tall building clusters impacts.

Relevant urban scalar dispersion literature focuses on either the effects of a tall building surrounded by low-rise buildings (e.g., Fuka et al., 2018; Heist et al., 2009; Brixey et al., 2009; Hertwig et al., 2019; Melo et al., 2023; Rich and Vanderwel, 2024) or on large building arrays or entire canopies (e.g., Arnold et al., 2004; Hertwig et al., 2018; Goulart et al., 2016; Coceal et al., 2014; Marucci and Carpentieri, 2020). For example, the DIPLOS project used wind-tunnel experiments, LES and direct numerical simulation (DNS) (Castro et al., 2017; Hertwig et al., 2018; Fuka et al., 2018) to address street network scale dispersion processes for cases with homogenous rectangular buildings and for isolated tall buildings. These enhance both understanding of key dispersion processes at this scale and development of simplified street network models (Cezana et al., 2021; Auerswald et al., 2024).

Thus, investigations of wind fields and/or scalar dispersion around real-city groups of tall buildings are scarce, and limited to simple layouts (aligned or staggered), with exception including Han et al. (2017) and Lim et al. (2022). Here we start to address this gap by considering a cluster of tall buildings using its real-world layout (see Fig. 1). We consider both the wind patterns and the dispersion fields induced by this cluster. We consider tall buildings when within a nearly neutral urban boundary layer (UBL), to address three questions: (1) Is it feasible to generate appropriate synthetic inflow turbulence for numerically simulating this UBL for a range of integral time scales? (2) For a group of tall buildings, how should we quantify the representative characteristic length scales? (3) What are the major impacts of a cluster of tall buildings on modulating the flow, turbulence, and scalar plume as they pass over it?

Here we focus on the tall buildings in City of London (Section 2). Our investigation uses both numerical and wind-tunnel approaches (Section 3), considering 7 wind directions (Section 3.4), whose results are analysed (Section 4) prior to our concluding remarks (Section 6).

2. Study area

For this work, we consider a cluster of 17 buildings within the City of London (Fig. 1) with heights between 80 m and 267 m. Their mean height is 140 m. With a ground-level mean building width of 45 m, the building height-width aspect ratio (AR) is within CTBU's TB values of 3 to 8. Considering only the 17 tall buildings, contained within a 700 m diameter, gives a plan area or packing density of $\lambda_p \approx 9\%$. To facilitate both laboratory experiments and numerical simulations (Section 3), a simplified representation of the 17 buildings is used (Fig. 1a) compared to reality (Fig. 1b).

Given the range of wind speed measured (Section 3.1), the full-scale Reynolds number can be more than 4.0×10^7 based on the ground-level mean building width and freestream velocity. As such high Reynolds numbers remain unattainable within wind tunnels,

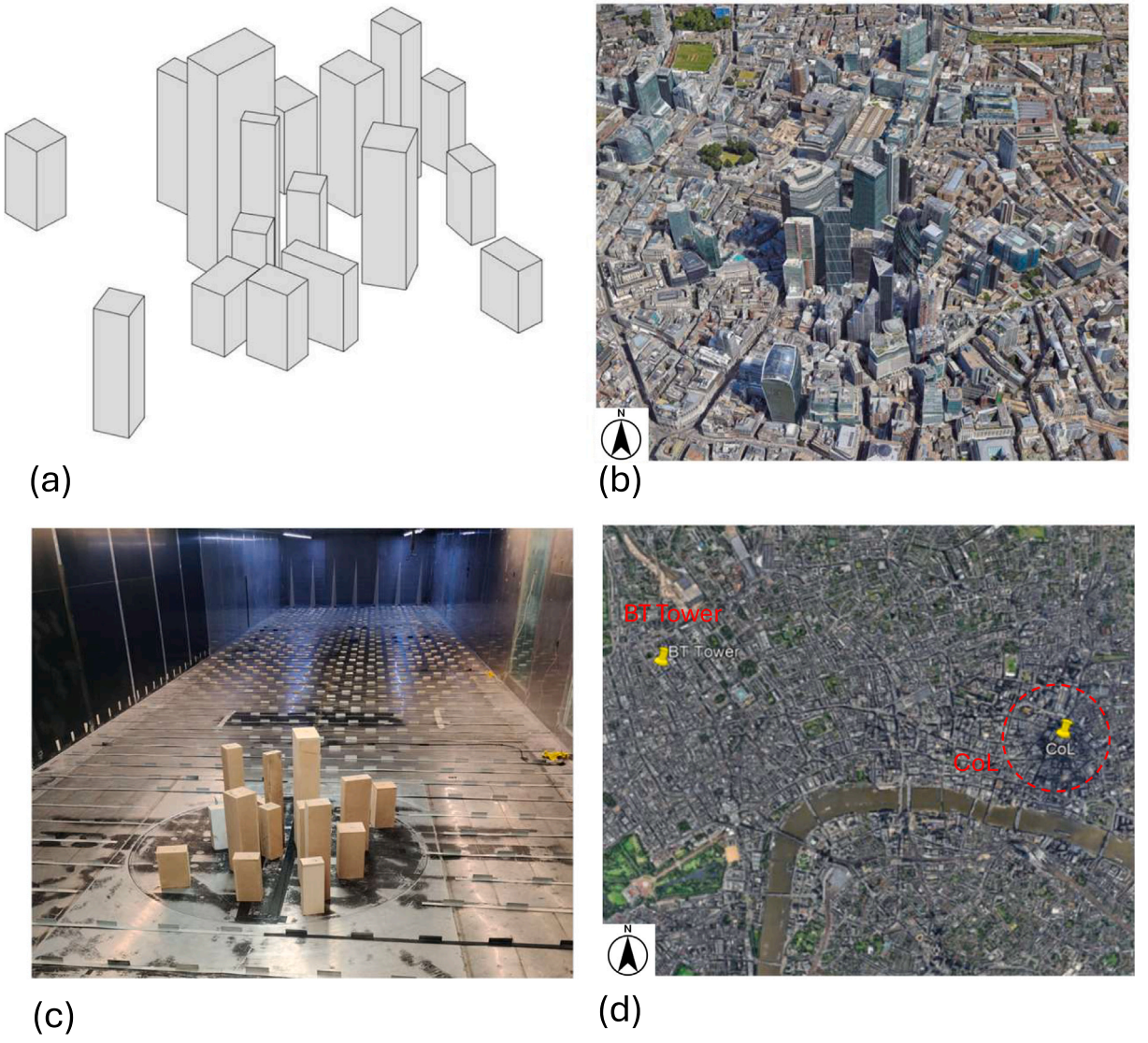

Fig. 1. Oblique view of 17 tall buildings in the City of London (centre is at 51°30′53.43″N and 0°4′54.29″W): (a) simplified and (b) actual area. (c) 1:500 scale model used in the EnFlo wind tunnel with dimensions detailed in Table 1. (d) Top view of the BT Tower and City of London areas, with the dashed-line circle marking the cluster area of $W_A = 700$ m in diameter detailed in Fig. 5.
Source: Google Maps.

we modify building geometries to ensure Reynolds-number-independent flow behaviour. A widely accepted approach to mitigate Reynolds number effects is to employ bluff bodies with sharp edges, which enforce fixed flow separation points regardless of viscous effects, thereby preserving a weakened form of dynamic similarity (e.g., Rodi, 1997; Xie and Castro, 2006). This methodology is broadly supported in the literature (e.g., Lim et al., 2022). Bearman and Morel (1983) noted that the incoming turbulence leads the flow in the shear layer over a bluff body to a rapid transition to turbulence, resulting in a larger effective Reynolds number. Castro and Robins (1977) and Plate (1999) demonstrated that Reynolds-number-independent results can be achieved when the Reynolds number based on the building width exceeds 5000–20,000, depending on model geometry. In the present study, the Reynolds number is approximately $Re_b = 1.2 \times 10^4$ based on the average building width b at laboratory scale (see Section 3.2) and the freestream velocity U_∞, which is sufficiently large to avoid dynamic similarity issues. Thus, our wind tunnel experiments are expected to reliably replicate the turbulent flow characteristics of the full-scale scenario.

We remove the building façades architectural details, as they are considered insignificant at the scales investigated. Such details are below the spatial resolution of both the laboratory sensors and the LES numerical grid, hence have a negligible influence on the resolved flow field (Arnold et al., 2004). Therefore, each building was simplified to a cuboid (Fig. 1a) with the same cross-sectional area as the real counterpart (Fig. 1b).

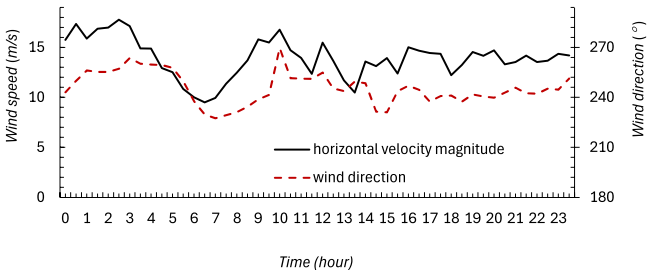

Fig. 2. Wind speed and directions at BT tower (Fig. 1) 191 m AGL on 12th March 2020 (30 min mean). Time is UTC shown time ending (06:30:01–07:00 shown at 07:00).

Real-world atmospheric boundary layers are turbulent and diurnally dynamic (e.g. Lean et al., 2019; Ayet and Katul, 2020). At the leading edge of a city's built surfaces with changes in surface roughness and energy balance heat flux partitioning, the new internal boundary layer that develops is referred to as urban boundary layer (UBL). The UBL is one of the most complex and least understood surface-atmosphere feedbacks, despite it being critical given both rapid urbanisation and climate change (Barlow, 2014). Dynamic UBL characteristics, including velocity gradient, turbulence intensity and integral length scales, thermal stratification, and boundary layer thickness, both influence and respond to the changing flow crossing the urban morphology. The surface is described using attributes such as packing density (plan area index) λ_p, frontal area index λ_f, and building aspect ratio of the buildings, roughness length and displacement height. Given their critical role in urban flow dynamics and pollutant dispersion, these parameters are extensively studied (e.g., Stull, 2016; Xie et al., 2004; Marucci et al., 2018; Sessa et al., 2020; MacGarry et al., 2025; Mishra et al., 2023).

The average building height in the surrounding area is approximately 22 metres (Xie and Castro, 2009), on an area that is approximately 10 m above sea level (ASL) (variation < 10 m). The centre of the study area is about 900 m from the centre of the Thames River, which is at sea level. The approaching UBL to the CoL under most wind directions can reasonably be treated as fully developed (Kotthaus and Grimmond, 2018; Hertwig et al., 2021; Warren et al., 2022), when the timescale of non-stationary wind fluctuations is assumed to greatly exceed the turbulence integral timescale. The former is typically associated with mesoscale or submeso-scale (Mahrt, 2009) motions. The integral time scale is critical for numerical weather prediction models closure schemes (Ayet and Katul, 2020), coupling between the meso- and micro-scale simulations (Kadasch et al., 2021), and synthetic inflow turbulence generation (Xie and Castro, 2008). However, as identifying energy spectrum separation between mesoscale and turbulent motions remains a challenge, creating uncertainty in estimating the integral time and length scales.

A common approach to estimating the integral time scale (Kaimal and Finnigan, 1994; Lewalle and Ashpis, 2004; Ayet and Katul, 2020) is to identify the frequency corresponding to the peak of the frequency-weighted power spectrum, $fE(f)$, where f is the frequency and $E(f)$ is the power spectral density, which can be calculated from the horizontal velocity measured at one station. Lean et al. (2019) reported a peak in $fE(f)$ at $f = 4.0 \times 10^{-3}$ Hz for turbulence measured at 191 m above ground level (on the BT Tower) in central London, giving an integral time scale of approximately 4-min. This is consistent with previous studies, such as 1-min observed in rural boundary layers (Mahrt, 2009) and LES of UBL (Xie, 2011).

Estimating the UBL integral length scales poses a greater challenge (Robins, 1979; Nandi and Yeo, 2021) as they are typically estimated using Taylor's hypothesis based on integral time scales derived from single-point measurements. Within and immediately above the urban canopy, where the fluctuating velocities are comparable to the flow convection velocity, Taylor's hypothesis may not hold. Nandi and Yeo (2021) compared streamwise velocity integral length scales (L_x) for neutral Atmospheric Boundary Layers (ABL) using various methods. ASCE 7–16, AIJ (2024), and Eurocode (2005) suggest L_x values of less than 300 m at a height of $z = 200$. ESDU 850202 (2001) provides a higher estimate ($L_x \approx 500$) m at the same height for a wind speed of 20 ms^{-1}. Hence, given the substantial variability in estimates there is a need for further investigation.

3. Methods

3.1. Real-world wind conditions

As the approaching wind conditions significantly affect the flow behaviour around tall building clusters and exhibit dynamic characteristics, we restrict our analysis to near-stationary and near thermally-neutral wind conditions, based on observations from the BT Tower located approximately 4 km northwest of the City of London (Fig. 1d). The wind data was sampled at 20 Hz with a 3D sonic anemometer (R3-50, Gill Instruments)(Figs. 2–4), measured at a height of $z = 191$ m above ground level from 0:00 to 23:59 on 12 March 2020 (Wood et al., 2010; Lean et al., 2019; Theeuwes et al., 2025). This provides a high-quality dataset suitable for analysing the relevant approaching boundary layer of interest herein. The single day – 12th March 2020 – was selected by using data created by Theeuwes et al. (2025) to filter for an approaching urban boundary layer with (a) near-neutral conditions (i.e. $-0.1 < (z-d)/L < 0.1$, where L is the Monin–Obukhov length, and $d = 11$ m is the displacement height), and (b) a "moderate to deep" boundary layer, i.e. no lower than 500 m. This lower limit was chosen as being approximately twice the maximum building

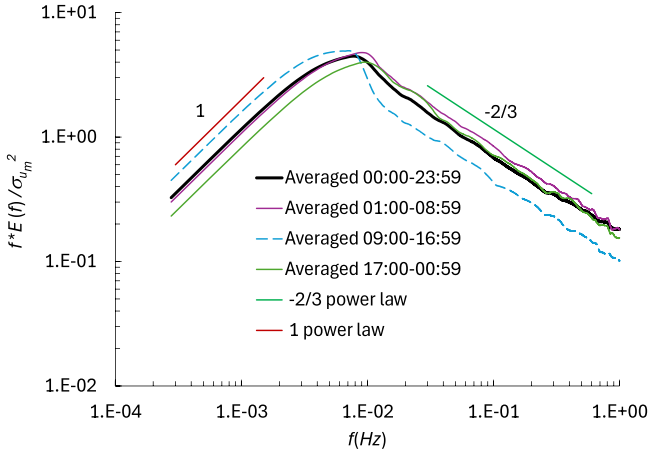

Fig. 3. The dimensionless frequency-weighted power spectrum $fE(f)$ with frequency f for 12 March 2020 derived hourly analysis of 20 Hz data observed at the BT tower (z = 191 m). Data bin average into 4 periods (00 : 00 – 23 : 59, 01 : 00 – 08 : 59, 09 : 00 – 16 : 59, 17 : 00 – 00 : 59), with 1 and −2/3 slopes shown.

height in the CoL cluster (Fig. 1) whilst ensuring that the BT Tower (sensor height z = 191 m) was always located within the atmospheric boundary layer. On this day winds are from the SW with the mean wind speed of 14 m s^{-1} (Fig. 2), well above the average of 8 m s^{-1} reported in Wood et al. (2010), consistent with the near-neutral condition. The wind speed and direction were more consistent after 09:00 than earlier in the day (Fig. 2).

As during 06:00–06:59 and 10:00–10:59 the hourly stability is non-neutral, we exclude these data from spectral analysis and estimation of the integral time scale. Hourly analysis of the 20 Hz $u(t)$ and $v(t)$ were carried out to calculate the horizontal velocity magnitude $u_m(t)$, its variance of $u_m(t)$ and the corresponding dimensionless frequency-weighted power spectrum, $fE(f)/\sigma^2_{u_m}$ (Fig. 3). The 22 spectra have similar shapes, with daytime (09:00 and 16:00) spectral peak being slightly shifted towards lower frequencies, attributed to the deeper daytime boundary layer, which varied between 800 and 1000 m.

The 22 spectra are categorised into three stability periods: Group 1 (01:00–08:59), Group 2 (09:00–16:59), and Group 3 (17:00–00:59). The profiles have a wide inertial subrange with a slope −2/3 at 0.02 Hz ≤ f ≤ 1 Hz, and a peak f_p approximately 0.01 Hz. The latter suggests an integral time scale $T_{int} \approx 1/f_p = 100$ s (Leonard, 1979; Kaimal and Finnigan, 1994; Ayet and Katul, 2020), consistent with the 4-minute time scale derived from BT Tower observations for a different day (Lean et al., 2019), as well as the 1-minute integral time scale observed in rural boundary layers (Mahrt, 2009). The spectrum at frequencies greater than 1 Hz shows a slower slope and is not shown. This is due to the spectrum aliasing occurring at frequencies close to the sampling frequency.

The relationship between the integral time scale and the frequency f_p for the maximum in $f_pS(f_p)$ depends on the shape of the spectrum. The standard von Karman spectrum for the u-component of isotropic turbulence (Diederich and Drischler, 1957) gives,

$$L_x = 0.145U/f_p, \tag{1}$$

where U is the local mean streamwise velocity. Given the mean streamwise velocity was approximately 14 ms^{-1}, and $f_p = 0.01$, the integral length scale in the streamwise direction is approximately 204 m. As the urban boundary layer flow is inherently anisotropic, a large degree of uncertainty must be considered when applying such a length scale.

Following Kaimal et al. (1972), the non-dimensional peak frequency is defined as

$$n_p = \frac{f_p z}{U}, \tag{2}$$

where z is the measurement height and U is the local undisturbed mean streamwise velocity. Kaimal et al. (1972) observed that n_p is independent of both z and U under neutral stability conditions. Combining Eqs. (1) and (2) yields

$$n_p = 0.145\,\frac{z}{L_x}. \tag{3}$$

Since n_p remains approximately constant in the neutral surface-layer observations from the Kansas experiment (Kaimal et al., 1972), Eq. (3) implies that the integral length scale L_x is linearly proportional to the height z. This behaviour is analogous to the classical assumption that the mixing length grows proportionally with the wall-normal distance in neutral surface layers (Stull, 2012). In the Kansas data, Kaimal et al. (1972) reported n_p = 0.045 and 0.25 for the u and v velocity components, respectively. The ESDU formulation gives n_p = 0.058 based on the BT Tower height, while ASCE 7–16, AIJ (2024), and Eurocode (2005) all yield n_p = 0.097. Using the BT Tower measurements and Eq. (2), we obtain n_p = 0.14, which lies between the Kansas values for the u and v components. It should also be noted that the BT Tower spectrum was estimated using the magnitude of the horizontal velocity components, $\sqrt{u^2+v^2}$. Finally, in the outer region of the atmospheric boundary layer, the turbulent length scale no longer increases linearly

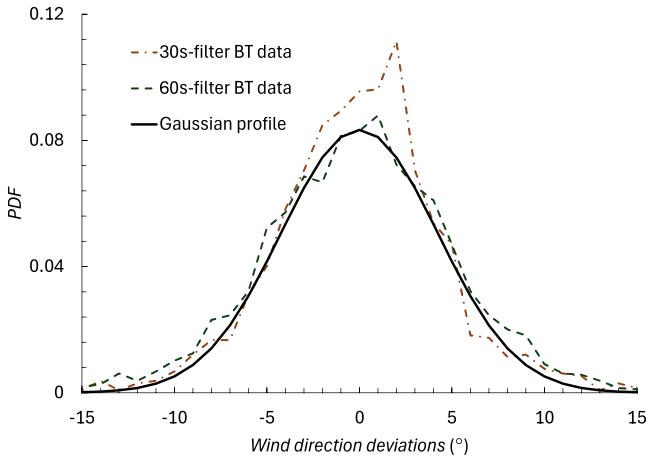

Fig. 4. Bin-averaged probability density distributions of wind direction difference from 30-min mean, derived from 44 30-min periods sampled into 30-s and 60-s means from 20 Hz observation at BT Tower on 12 March 2020. A Gaussian distribution with a deviation $\sigma_\alpha = 3°$ is shown for reference.

with wall-normal distance. Since the top of the BT Tower is located near the interface between the surface and outer layers, some discrepancy in the observed value of n_p is therefore expected.

Given the integral time scale of ~2 min and the width of the CoL of ~ 700 m (Fig. 1), it is useful to quantify the wind direction variability within 30 mins. As 30-min (or longer) period is commonly used for determining eddy covariance fluxes (Wood et al., 2010; Grimmond and Ward, 2021; Mauder et al., 2021), whereas 10-min is typically employed for wind-related applications (Eurocode, 2005), we compare variability in results for 15- and 30-min averaging periods. Under these close to neutral conditions (i.e. strong consistent winds) there is a negligible difference. Under a wider range of meteorological conditions more variability occurs (e.g. Kent et al., 2017). The high-frequency observations are resampled to 60-s and 30-s means (Xie, 2011) to remove most turbulent fluctuations, including those higher frequencies within the inertial subrange.

To ensure statistical convergence, the 22-hour velocity time series was divided into 44 segments, each of 30 min in duration. Probability density functions (PDFs) of wind direction difference from the 30-min means were calculated from the segments, and their averages of the 44 PDFs are shown in Fig. 4. The difference between the two profiles using 30-second and 60-second filtered velocity time series is small.

3.2. Wind tunnel experiments

The University of Surrey Environmental Flow (EnFlo) wind tunnel is used to conduct experiments using a 1:500 scale model of the CoL cluster (Fig. 1c). This suck-down tunnel with two fans mounted at the exit is 20 m long, 3.5 m wide, and 1.5 m high, with a maximum achievable freestream velocity of 5 ms^{-1} (Castro et al., 2017). For this study, the freestream velocity (U_∞) is set at 2 ms^{-1}. An artificially thickened boundary layer is obtained using 7 Irwin spires (separation = 500 mm) located at the tunnel inlet. The boundary layer height ($\delta = 1$ m) depends mostly on the spire's height once it has fully adjusted to the underlying wall surface. The resulting Reynolds number, based on U_∞ and δ, is $Re_\delta = 1.32 \times 10^5$.

To mimic the Reynold shear stress profile of the full scale atmospheric boundary layer, the spires are followed by staggered roughness elements (20 mm high and 80 mm wide) throughout the tunnel. The distance between each roughness elements is 160 mm laterally and 240 mm in the streamwise direction. The CoL models are placed on a circular turntable, located 14 m from the inlet. The rotatable turntable (diameter 1400 mm) allows different wind directions to be observed with respect to the 1:500 scale CoL cluster model (Fig. 1c).

To measure the three components of the velocity simultaneously at each point downstream of the cluster, a Dantec Dynamics FibreFlow 3D laser Doppler anemometry (LDA) is used. Data are sampled at approximately 100 Hz for 1 min. An in-house ultrasonic mist generator provides an aerosol solution of sugar tracing particles (Castro et al., 2017; Mishra et al., 2024). The particle's mean diameter is about 1 μm. A 100% propane gas is released from a ground-level pipe (internal diameter = 2 mm, flow rate = 26 ml/min). The propane concentration is measured with a Cambustion HFR500 fast flame ionisation detector system (FFID), with a gas sample being suck into the chamber through a transfer tube. To not interfere with the flow, the sampling point is 4 mm downstream of the LDA measuring volume. More details are provided, with measurement uncertainties associated with scalar fluxes and flow field given in Marucci and Carpentieri (2019). The FFID/LDA probes are mounted on a traverse that can move freely in all three Cartesian directions.

The choice of coordinate system origin is somewhat arbitrary. Here it is fixed close to the tallest building, so the cluster extent is similar in all directions (Fig. 5). The distance of the buildings from the centre is normalised with the cluster width. For the experimental data, two Cartesian coordinate systems are used, (a) a geographical (x_g: west-east, y_g: south-north, z_g: vertical), and

Table 1
Real-world dimensions and orientations of the buildings included in the 1:500 model (Fig. 5).

Building No	Length (m)	Width (m)	Height (m)	Centre (x_g) (m)	Centre (y_g) (m)	Orientation (deg)
1	82.3	28	101	82.55	−81.72	−19.9
2	54.8	39	99.2	47.87	−133.51	−21.2
3	66.6	44	80	−15.86	−113.24	69.2
4	44.4	42	160	−85.83	−309.38	−97.9
5	85.9	48.5	267	−51.206	45.55	57.5
6	61	35	81	276.92	6.2	−33.3
7	50	50	180	127	51.887	0
8	37	37	120	38.87	29.897	1.5
9	50.5	31	95	191.32	158.7	−42.9
10	53.7	45	174	49.74	−184.2	−30
11	44	33	202	84.064	244.78	−27.7
12	41	27	109	128.2	280.13	−27.8
13	53.7	48.2	108	−33.53	210.98	−33.9
14	61	29.5	173	−122.7	129.1	−25.5
15	50	44	104	−278.93	69.496	−31.9
16	39	18.7	223	−3.87	−9.71	0
17	39	34.8	104	−3.87	−40.09	0

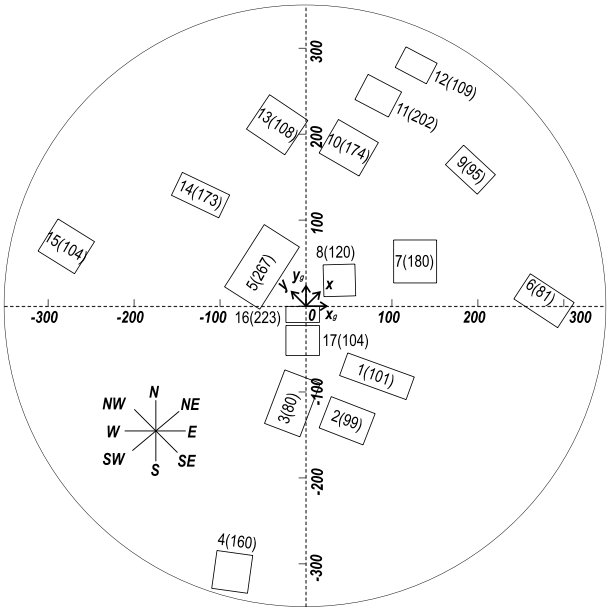

Fig. 5. Plan view of the full-scale, simplified CoL building cluster model with geo-located coordinates (metre, x_g west to east, y_g south to north and z_g ground vertically) with building number (Table 1) and height (metres). Local model or wind tunnel coordinates (x, y, z) are with x in the streamwise direction. The solid circle indicates the cluster area, which has a diameter of W_A = 700 m.

(b) local (x: direction of the flow or streamwise, y: follows the right-hand rule, z: vertical). z_g and z are identical. The building locations in the Cartesian coordinate system are shown in Fig. 5. The building dimensions, centre locations in the x–y plane and their orientation relative to the x axis are given in Table 1. A counterclockwise direction is taken as positive.

The 1:500 CoL model has a lateral cluster width (W_A) of ~1400 mm, with tallest building 534 mm and the shortest building 160 mm. The mean height (H_{ave}) of the cluster is 288 mm, calculated using the cross-sectional area A_i,

$$H_{ave} = \sum_{i=1}^{17} A_i h_i / \sum_{i=1}^{17} A_i, \tag{4}$$

where h_i is the height of the i_{th} building. The source for the concentration measurement was placed at ($x = -1.25W_A, y = 0, z = 0$), $1.25W_A$ upstream of the cluster centre for all wind directions. Lateral profiles of the velocity and concentration were measured at the mid-height of the cluster ($z = 0.5H_{ave}$), while vertical profiles were measured at ($x > 0.5W_A$, $y = 0$). All measurements in the wind tunnel were recorded in the local coordinate system (x, y, z). The turntable was rotated by the required amount to simulate the required wind direction.

3.3. Large-eddy simulation (LES)

The parallel LES model embedded in the open-source package PALM-4U (Maronga et al., 2015) is used to compute the urban boundary layer flow. This uses the filtered continuity and Navier–Stokes equations:

$$\frac{\partial u_i}{\partial x_i} = 0 \tag{5}$$

$$\frac{\partial u_i}{\partial t} + \frac{\partial u_i u_j}{\partial x_j} = -\frac{1}{\rho}\frac{\partial p}{\partial x_i} + \nu\frac{\partial^2 u_i}{\partial x_j \partial x_j} - \frac{\partial \tau_{ij}}{\rho \partial x_j}, \tag{6}$$

where u_i and p represent the resolved (or filtered) velocity and pressure, respectively; ν is the kinematic viscosity; ρ is the air density; and τ_{ij} denotes the subgrid-scale (SGS) stress. The PALM-4U code employs a 1.5-order (Deardorff, 1980) turbulence closure model to parameterise the SGS stresses. In this model, an additional transport equation for the SGS turbulent kinetic energy e is solved. The closure is based on the Boussinesq hypothesis, where the SGS stresses τ_{ij} are assumed to be proportional to the local gradients of the resolved velocity field u_i, modulated by an eddy viscosity K_m. Xie and Castro (2006) note that the turbulence scales of flows around a sharp-edged bluff body are governed by the bluff body size, and the numerically generated flow data are generally insensitive to the specific SGS model employed, providing that the computational grid sufficiently resolves the inertial subrange of the turbulent spectrum.

The filtered transport equation of scalar concentration is written as,

$$\frac{\partial c}{\partial t} + \frac{\partial u_j c}{\partial x_j} = \frac{\partial}{\partial x_j}\left[(D + K_s)\frac{\partial c}{\partial x_j}\right], \tag{7}$$

where c denotes the resolved-scale scalar concentration, D is the molecular diffusivity of the scalar, and K_s is the SGS eddy diffusivity for scalars. The estimation of the SGS eddy diffusivities (K_m for momentum and K_s), are linked to e and SGS mixing length l. Under neutral thermal stratification, l is a function of height z and grid size Δ (Maronga et al., 2015).

The PALM-4U synthetic inflow turbulence generator (STG) (Kadasch et al., 2021) is used at the LES domain inlet. It is a hybrid between the forward stepwise method (Kim et al., 2011) and digital filtering technique (Klein et al., 2003) based on an exponential correlation function suggested by Xie and Castro (2008), with inlet flow-rate correction (Kim et al., 2013). Turbulent inflow conditions are generated based on prescribed mean streamwise velocity, turbulent stresses, and turbulence integral length scales, assuming homogeneity in the spanwise direction. Herein, the mean velocity and turbulent stress profiles of the incoming turbulent boundary layer are derived from observations taken in the University of Surrey Environmental Flow (EnFlo) wind tunnel (e.g. Castro et al., 2017).

The integral time and length scales in the streamwise, spanwise, and vertical directions are set to $T_{int} = 240\,\text{s}$, $L_y = 60\,\text{m}$, and $L_z = 60\,\text{m}$, respectively. The integral time scale T is within the range derived from BT Tower observations (Fig. 3 and Lean et al. (2019)). Given such flows are insensitive to the Reynolds number, a freestream speed of 2.8 ms^{-1} is used for the LES. Based on Taylor's hypothesis, the streamwise integral length scale L_x at $z \leq 191\,\text{m}$ is estimated between 0 and 672 m. However as T, rather than L_x, is typically used in synthetic inflow turbulence generation, using Taylor's hypothesis is inaccurate, and using it for urban boundary layer flows with anisotropy can lead to large discrepancies. Xie and Castro (2008) demonstrate turbulent stresses are relatively insensitive to the inflow integral length scales when they have the same order of magnitude as the building width. Hence, suggesting testing effects of inflow integral time and length scales is deemed unnecessary for this work.

The LES full-scale computational domain dimensions are $\mathcal{L}_x = 4320\,\text{m}$ (streamwise), $\mathcal{L}_y = 4224\,\text{m}$ (spanwise), and $\mathcal{L}_z = 500\,\text{m}$ (vertical), with the inlet at 1500 m upstream of the cluster's leading edge (approximately $10H_{\text{ave}}$). These dimensions ensure sufficient upstream development of the approaching flow (MacGarry et al., 2025) and allow for the evolution of wakes and plumes downstream. Since the focus is on the effects of a tall building cluster, any minor development of mean flow and turbulence near the wall downstream of the inlet is not expected to significantly influence the results. The inflow boundary depth has an LES to wind tunnel ratio of 500:1. A periodic boundary condition at the two lateral boundaries, a stress-free boundary condition at the top, a solid wall boundary condition, and a radiation boundary condition at the outlet were used. The Cartesian mesh employed has a uniform resolution of 2 m in the horizontal and 2.5 m in the vertical directions. Xie and Castro (2006) recommend a grid resolution of $b/16$ (where b is the building width) as adequate for accurately predicting form drag coefficients and turbulent stresses. This is consistent with MacGarry et al. (2025) finding a strong agreement in turbulent stresses when using both a coarser ($b/10$) and a finer mesh ($b/20$) for a large array of idealised tall buildings. Here, with an average building width for the City of London cluster of $b \approx 44$ m, the mesh is finer than both prior studies. To ensure consistency across simulation cases, the model geometry, computational domain and mesh are kept identical for different wind directions. A Courant–Friedrichs–Lewy (CFL) number of 0.9 was selected, resulting in an average time step of approximately 1.00 s. The initial flow development period was set to $T_{ini} = 10$ h of simulated flow time. Statistical averaging for turbulence and scalar concentration fields was performed over a subsequent duration of $T_{ave} = 20$ h. The dimensionless averaging time, $U_\infty T_{ave}/\mathcal{L}_z$, is ≈140. The ground-level source was positioned at $(x = -1.25W_A,\ y = 0)$, consistent with the configuration used in the physical experiments.

Table 2
City of London cluster simulation cases differ with wind direction.

Cases	A	B	C	D	E	F	G
Wind direction	NE 45°	SE 135°	SSW 215°	SW 225°	SWW 235°	W 270°	NW 315°

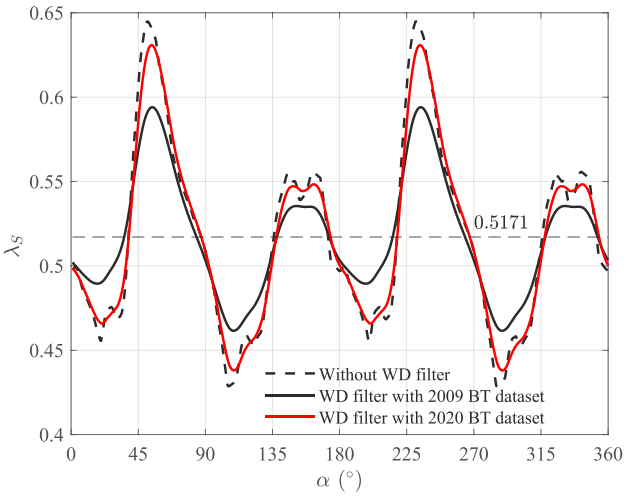

Fig. 6. Variations of the solidity, λ_s, of the CoL cluster with mean ($\overline{\lambda}_s$ of 0.52, dashed). The 2009 BT Tower observations were sampled for 3 June 2004 (Wood et al., 2009; Xie, 2011).

3.4. Case studies and evaluation

7 cases are simulated by wind tunnel and LES, which vary with wind direction (Table 2). For the SSW, SW, SWW, and NW wind cases, the LES coordinate system coincides with the (x, y, z) coordinates shown in Fig. 5. For the NE and SE wind cases, the building cluster model is rotated 180° clockwise about the z axis, while the (x, y, z) coordinate system remains fixed within the LES computational domain.

As the 17 tall buildings are densely packed, their joint aerodynamic impact can be greater than any individual building alone. Following Burian et al. (2002) and Wong et al. (2010) we estimate frontal area index (λ_f) by assessing the total area of building facets projected to a plane perpendicular to the wind direction, with variations (e.g. Fig. 4) needing to be accounted for. Here, we introduce a cluster solidity (λ_s) to help quantify the cluster effect on dominant vortex shedding:

$$\lambda_s(\theta) = \int_{-\infty}^{+\infty} \mathcal{F}(\theta', \theta)\psi(\theta - \theta')\, d\theta', \tag{8}$$

where

$$\mathcal{F}(\theta', \theta) = \begin{cases} \mathcal{PDF}(\theta - \theta') & \text{if } |\theta - \theta'| \le 90°, \\ 0 & \text{otherwise}, \end{cases}$$

and

$$\psi(\theta) = \frac{1}{H}\int_0^H \frac{L_s(z, \theta)}{L(z_0, \theta)} dz.$$

The probability density distribution of wind direction $\mathcal{PDF}(\theta - \theta')$ is derived from 30-min mean wind direction (see Fig. 4), where $\psi(\theta)$ is the local solid ratio at a wind direction θ, H is the height of the tallest building in the CoL cluster, $L_s(z, \theta)$ is the projected length of the solid part for a wind direction θ at height level z, and $L(z_0, \theta)$ is the width of the cluster for a wind direction θ at ground level $z = 0$.

The mean solidity over all possible wind angles ($0 - 360°$) is $\overline{\lambda}_s = 0.52$ (Fig. 4). As noted the 12 March 2020 had close to neutral conditions with low variability in direction ($\sigma = 3°$, Fig. 2), the wind tunnel and LES both assume strictly stationary wind conditions, set to match BT Tower observations. Accounting for wind direction variability does alter the estimated cluster solidity for 12 March 2020 (red, Fig. 6). When the wind direction deviations observed on a second day (3 Jun 2004, Wood et al., 2009; Xie, 2011) that is more variable, the cluster solidity (black line, Fig. 6) differs. Based on the mean solidity $\overline{\lambda}_s$, an effective width of the cluster, $W_e = \overline{\lambda}_s W_A$.

Nguyen et al. (2023) note that "the conventional Fourier analysis is used to process a sufficiently long time series of a stationary process but can struggle to identify energetic and localised events in short time series". Given the complex interactions among the

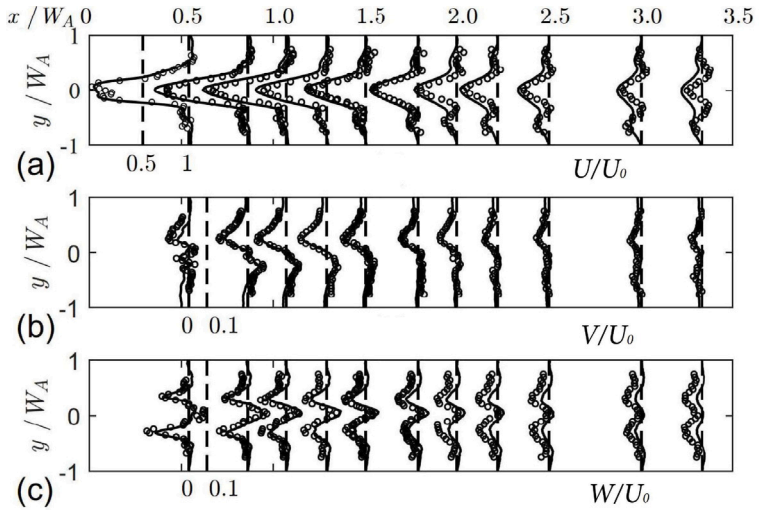

Fig. 7. Comparison for a SW wind direction at $z = 0.5H_{ave}$ between LES (lines) and wind tunnel (circles) of (a) mean streamwise velocity, (b) mean spanwise velocity, and (c) mean vertical velocity. Observations taken at 11 points downwind between $x/W_A = 0.54$ and 3.33.

vortices generated by individual buildings, and the resulting intricacy of the velocity time series, we employ the Morse wavelet in our wavelet analysis (Eqs. (9)–(10)) (e.g., Torrence and Compo, 1998; Olhede and Walden, 2002; Nguyen et al., 2023) to characterise the dominant frequency in the wake. This approach, rather than relying on the Fourier Transform (Perrier et al., 1995), enables identification of the dominant vortex-shedding frequency from the building cluster. A detailed description of the wavelet analysis is provided in Nguyen et al. (2023), with a brief summary included here,

$$\boldsymbol{\Phi}(a,t) = a^{-0.5}\int_{-T_1}^{T_2} \phi^*\left(\frac{\tau - t}{a}\right)\xi(\tau)\mathrm{d}\tau, \tag{9}$$

where $\xi(\tau)$ is a time series signal, $\boldsymbol{\Phi}$ is the wavelet coefficient, i.e. the scalogram, ϕ is the mother wavelet with the asterisk denoting the complex conjugate of the function. a and t are respectively the scale and translation (time) parameters. The Morse wavelet function is employed. The time-averaged wavelet magnitude is calculated,

$$\overline{\boldsymbol{\Phi}}(\tilde{f}) = \int_{-T_1}^{T_2} \left|\boldsymbol{\Phi}(\tilde{f},t)\right| \mathrm{d}t, \tag{10}$$

where $\tilde{f} = fW_e/U_\infty$ is dimensionless frequency, with $f = 1/(2a)$ and U_∞ being the freestream velocity. When referring to the dominant vortex shedding frequency of a building cluster, $\tilde{f}$ is commonly referred to as a Strouhal number *St*.

To demonstrate how the wind tunnel and LES vertical-profile values compare, we show the SW wind direction (Case D, Table 2) at 11 stations downwind of the cluster from $x/W_A = 0.54$ to 3.33 for streamwise, spanwise, and vertical mean velocities (Fig. 7) and turbulent stresses (Fig. 8). The reference velocity U_0 is measured at height $z = 0.5H_{\mathrm{ave}}$ in the same downstream position in the absence of the building cluster. In the near wake, $0.54 \le x/W_A < 2.5$, both mean and turbulent stresses show a good agreement. In the far wake ($x/W_A \ge 3.0$), LES under-predicts the magnitude of the variation in vertical velocity (Fig. 7c). Additionally, the LES under-predicts the streamwise turbulent stress downstream of $x/W_A = 1.5$ (Fig. 8c).

These discrepancies are likely attributable to the use of a simplified rough-wall model, the Monin–Obukhov similarity theory (MOST) (e.g. Mason and Thomson, 1992; Xie et al., 2004), despite the inflow turbulent boundary layer parameters being derived from experimental observations. A mismatch between the inflow conditions and the wall model can also lead to turbulence decay in the near-wall region (e.g. Richards and Norris, 2011), thereby reducing LES accuracy in the far field. Additionally, wind tunnel blockage effects may have contributed to the observed discrepancies, particularly in the far wake where the wake width increases and blockage effects become more pronounced. Nevertheless, the overall agreement between LES predictions and experimental data for both the mean flow and turbulent stresses is considered satisfactory.

Comparison of the LES and wind tunnel mean normalised concentration C^* between at $z = 0$, uses:

$$C^* = \frac{C\,U_0\,H_{\mathrm{ave}}^2}{Q}, \tag{11}$$

where C is the mean scalar concentration, and Q is the scalar emission rate. Overall, the LES near and far field predictions are in very good agreement with the wind tunnel FFID measurements (Fig. 9), indicating that the current full-scale LES is capable of accurately predicting mean concentrations resulting from a point source release.

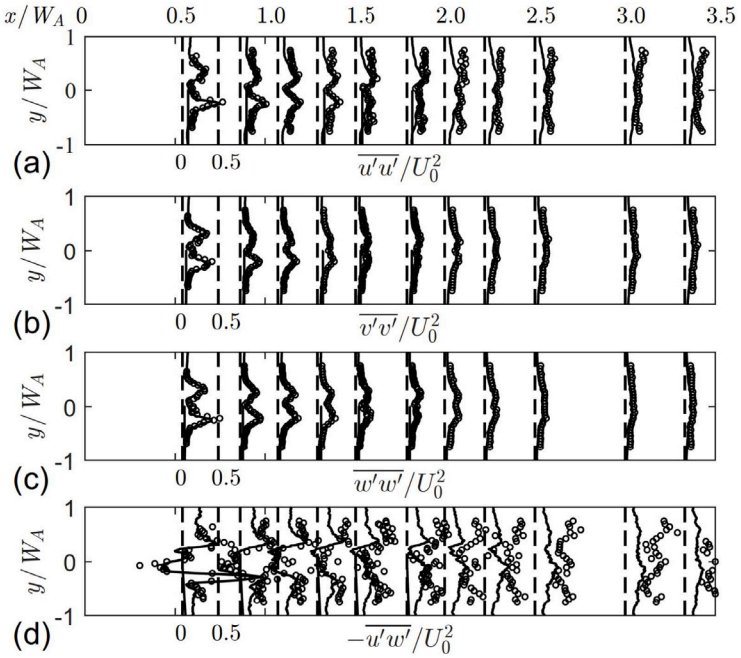

Fig. 8. A comparison between the LES and wind tunnel data at $z = 0.5H_{ave}$ in the SW wind for (a) $\overline{u'u'}/U_0^2$, (b) $\overline{v'v'}/U_0^2$, and (c) $\overline{w'w'}/U_0^2$. (d) $-\overline{u'w'}/U_0^2$ from LES. LES data (solid lines); Experimental data (circles).

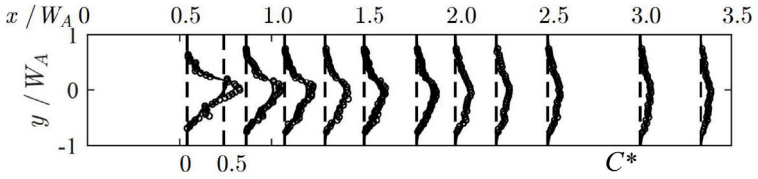

Fig. 9. As Fig. 8, but normalised mean concentration (Eq. (11)) at $z = 0$.

4. Results and discussion

4.1. Dominant vortex shedding frequency and wake

Although we do not investigate the interaction between the tall building cluster and the top of the boundary layer, such as the formation of an inversion layer there, in either the wind tunnel or LES. This could be crucial for future studies. Outside the wake region, the spectrum is very similar to the inflow spectrum shown in Fig. 3 (also see Xie and Castro (2008) and Xie (2011)), where a single dominant turbulent eddy frequency is indiscernible.

4.1.1. Dominant vortex shedding frequency

We consider the SW wind direction case, as it aligns with the orientation of the largest and tallest building in the cluster (Building 5, Fig. 5). The solidity λ attains its maximum at a wind direction close to $\alpha = 225°$, leading to a more pronounced wake deficit. Contours of the instantaneous vertical velocity w within the range $0.25 \leq z/H_{\text{ave}} \leq 1.0$ clearly reveal coherent flow structures of cluster scale W_A in the wake region (see Fig. 10b,c). Near the ground, for example at $z/H_{\text{ave}} = 0.125$, flow structures are still observable but noticeably weaker due to the dissipation associated with high turbulence intensity (see Fig. 10a). At $z/H_{\text{ave}} = 2$, a large flow structure, but smaller than the cluster scale W_A, is evident in the wake region (figure not shown), influenced by the presence of the 267 m-high building. Far above the cluster top, at $z/H_{\text{ave}} = 3$, large-scale flow structures become difficult to discern (see Fig. 10d).

The formation mechanism arises from the interaction between the incoming turbulent boundary layer and the vortices shed from individual tall buildings, as well as from vortex merging within the wake region (Han et al., 2017; Mishra et al., 2023; Nguyen et al., 2023; Mishra et al., 2024; Inam et al., 2026). These vortices are generated from both the building tops and the lateral façades. Park et al. (2015) reported the formation of strong streamwise vortices in the wake of an isolated high-rise building, which subsequently

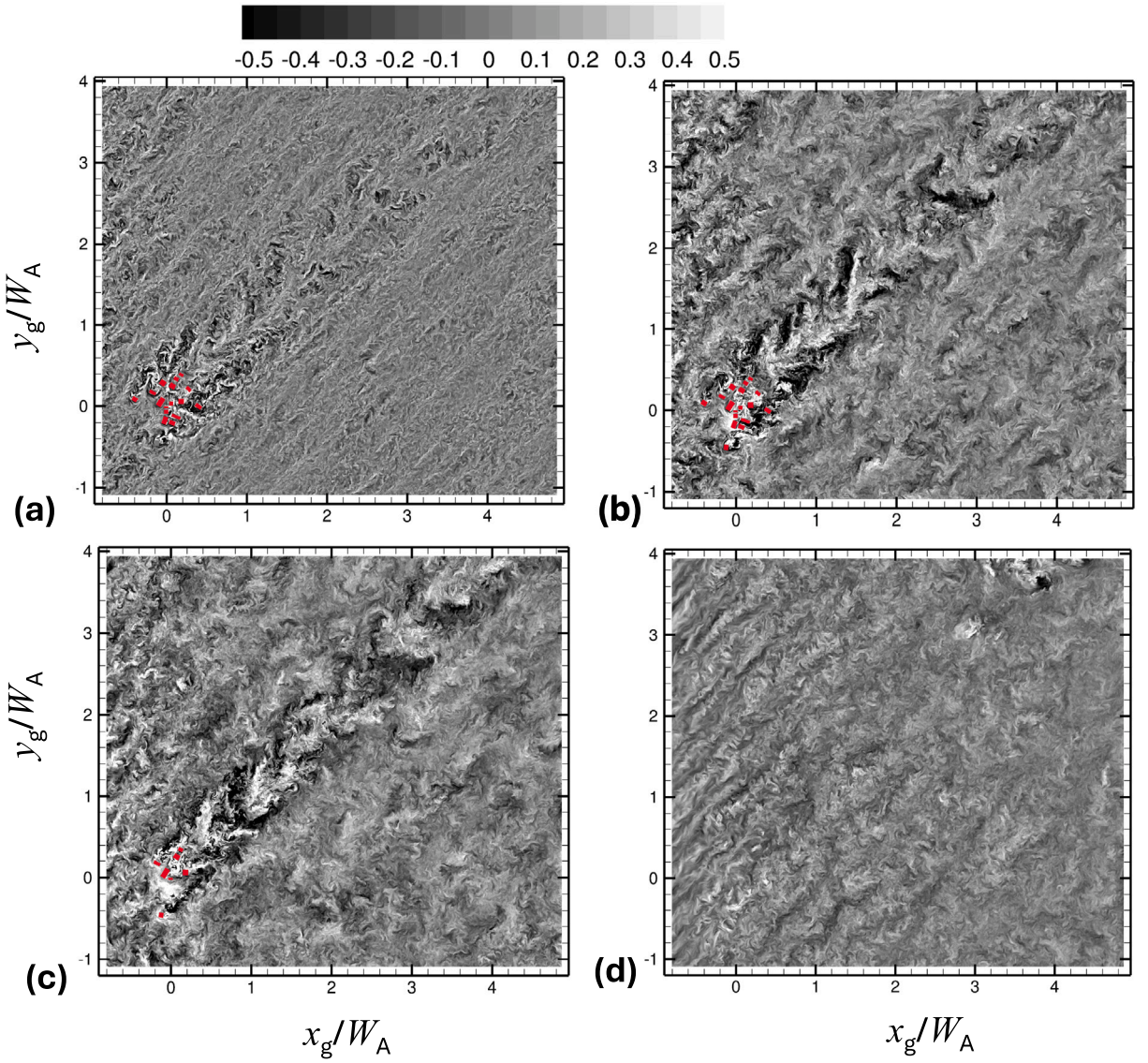

Fig. 10. Contours of the instantaneous vertical velocity w at $z/H_{ave} = 0.125$ (a), 0.5 (b), 1.0 (c), and 3.0 (d) for the SW wind direction. The centre of the tall-building cluster is located at ($x_g = 0$, $y_g = 0$). The red rectangles in the lower-left corner indicate the tall-building cluster.

enhanced the development of large turbulent structures. It is therefore reasonable to expect that a cluster of tall buildings would generate even larger and more energetic turbulent motions. Fig. 10b shows a chain of λ-shaped flow structures in the near-field wake, with characteristic sizes on the same order of magnitude as the cluster width W_A. Farther downstream, these structures gradually merge into larger coherent motions. However, because the cluster size is comparable to the atmospheric boundary-layer thickness, fully elucidating the underlying interaction mechanisms becomes extremely challenging.

To explore the LES wake region flow characteristics and vortex shedding dynamics, a number of probes are placed in the LES wake region. In the far wake of the cluster $(x/W_A, y/W_A) \geq (0.8, 0.8)$, the wakes originating from individual buildings merge along the wind direction, forming a single cluster wake. We use the dimensionless vortex shedding frequency (i.e. Strouhal number St) to discuss the global vortex shedding behaviour based on the fluctuating velocity fields in the wake. For this analysis we show the wavelet time-frequency scalogram (Fig. 11a) for the fluctuating spanwise velocity at ($x = 2.5W_A, y = 0, z = 0.5H_{ave}$), when the wind is from the SW, with the time-averaged wavelet magnitude $\overline{\Phi}(\tilde{f})$ (Fig. 11b) with the dominant dimensionless frequency $St = 0.136$, which is close to that of a single isolated square cylinder. The same Strouhal number of $St = 0.136$ is observed at the $z/H_{ave} = 0.5$ sampling locations within $1.5 \leq x/W_A \leq 4.5$ and $|y|/W_A < 0.15$ ranges, suggesting it is a representative Strouhal number for this cluster of vortex shedding.

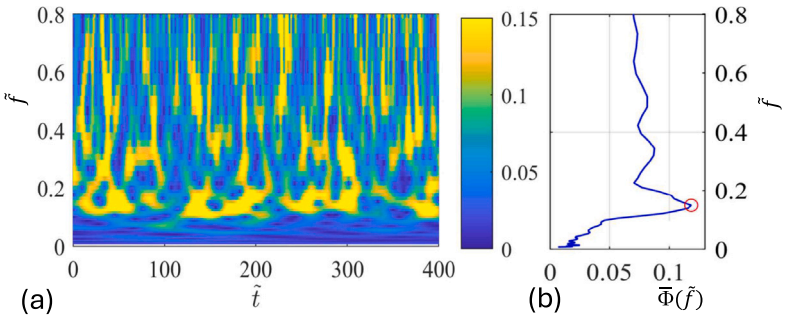

Fig. 11. Wavelet analysis of spanwise fluctuating velocity when wind from the SW at $x = 2.5W_A, y = 0, z = 0.5H_{ave}$, showing (a) the time-frequency scalogram map, and (b) time-averaged wavelet magnitude with dimensionless frequency $\tilde{f}$ for the primary vortex (red circle, Strouhal number $St = 0.136$), based on effective cluster width W_e and freestream velocity U_∞. Note $\tilde{t} = tU_\infty/W_e$ is dimensionless sampling time.

Nguyen et al. (2023) reported that the dominant vortex-shedding frequency from an array of 2 × 2 cylinders (with a very large height-to-width ratio) at various incidence angles in homogeneous inflow turbulence is governed by the array width, resulting in an array-width-based Strouhal number close to that of a single square cylinder. Inam et al. (2026) further investigated arrays of 2 × 2, 3 × 3, and 4 × 4 square cylinders with different spacings and collectively concluded that the vortex-shedding frequency is primarily governed by the array size. When corrected for array solidity, the Strouhal number of the vortex-shedding frequency approaches that of a single square cylinder. Mishra et al. (2024) experimentally studied arrays of 4 × 4 and 8 × 8 square cylinders with a height-to-width ratio of 4 and varying spacings in a turbulent boundary layer. The boundary-layer thickness-to-cylinder-height ratio was 4, similar to the current study. Mishra et al. (2024) noted that, provided one goes sufficiently downstream of a building cluster (in the far regime as defined in Mishra et al. 2023), the individual building wakes merge and an overall cluster wake scaling with the width of the cluster emerges. As a consequence, a single dominant shedding frequency emerges.

The dominant vortex-shedding frequency is approximately 10^{-3} Hz, corresponding to a Strouhal number of $St = 0.136$ (see Fig. 11). Using Taylor's hypothesis and a convection velocity based on the local streamwise mean velocity of 1.3 m/s at $(x_g/W_A, y_g/W_A, z_g/W_A) = (1.24, 0.88, 0.5)$, the characteristic length scale of the shed vortices is estimated to be about 1300 m. Considering the variations of the convection velocity in the near wake (see Fig. 7), this estimated length scale is reasonably regarded as being of the same order of magnitude as the λ-shaped structures observed in Fig. 10b. These turbulent structures do not fall within the range of the so-called "superstructures" in turbulent boundary layers (e.g. Hutchins and Marusic, 2007), which are significantly longer. This, together with the wake flow structures observed in Fig. 10 at different heights, collectively indicates that the flow dynamics are primarily governed by the tall-building cluster.

In contrast, when tall buildings are aggregated to form a very large cluster (approaching a canopy), as in MacGarry et al. (2025) who simulated an array of 144 rows of square cylinders with an average height-to-width ratio of 4 in a turbulent boundary layer and boundary-layer thickness six times the building height, no dominant vortex shedding was identified immediately above or within the canopy, or in the wake flow. This suggests that a shallow boundary layer, in terms of the thickness-to-building-height ratio, does not generate a dominant vortex.

4.1.2. Wakes behind the CoL cluster

To visualise the three-dimensional flow, we converted the PALM4U data from the NCAR netCDF raster format into Tecplot 3D Block format. The time-averaged velocity magnitude contours and streamlines at $z/H_{\text{ave}} = 0.5$ for the NW wind (Fig. 12a), reveal a clear anti-clockwise deflection of the primary wake flow. Given this anti-clockwise wake deflection induced by the building cluster under NW winds, the SE case was expected to produce a clockwise wake deflection by analogy with flow over a cambered aerofoil. However, this is difficult to discern in Fig. 12d, highlighting the complexity of wake interactions. Secondary recirculation regions are evident immediately downwind of the tallest and widest cuboid-shaped building, B5, whose long horizontal edge is nearly perpendicular to the NW and SE wind directions, as well as downwind of building B4, which exhibits the least interaction with the cluster and creates a channelling flow between B4 and the adjacent buildings.

For the SW wind (Fig. 12c), the wake centre aligns with the cluster centreline, and the primary recirculation region is nearly symmetric about the centreline. The ratio of the recirculation length (from the cluster centre to the streamline saddle point) to the cluster width W_A is approximately 0.8, which is smaller than the corresponding ratio for a single tall building, such as the CAARC building (e.g., Daniels et al., 2013), or a wall-mounted single cube in a boundary-layer flow (e.g., Castro and Robins, 1977). This is unsurprising, as a more comparable ratio of recirculation length to cluster width should account for the cluster's solidity. For the NE wind (Fig. 12b), the wake is less symmetric than in the SW case. The primary recirculation length is similar to that in the SW wind but contains two distinct secondary recirculation regions, underscoring the complexity of flow interactions within the wake.

To examine the vertical development of the wake flow, time-averaged velocity magnitude contours and streamlines, derived from the time-averaged velocities on a vertical along-wind cluster centre-plane ($y = 0$), are shown in Fig. 13 for the NW, NE, SE, and SW winds. A primary recirculation is not visible in the NW and SE wake flows on this vertical centre-plane. This observation is consistent with Fig. 12a, where the centre-plane lies outside the primary recirculation at half building height ($z/H_{\text{ave}} = 0.5$), and

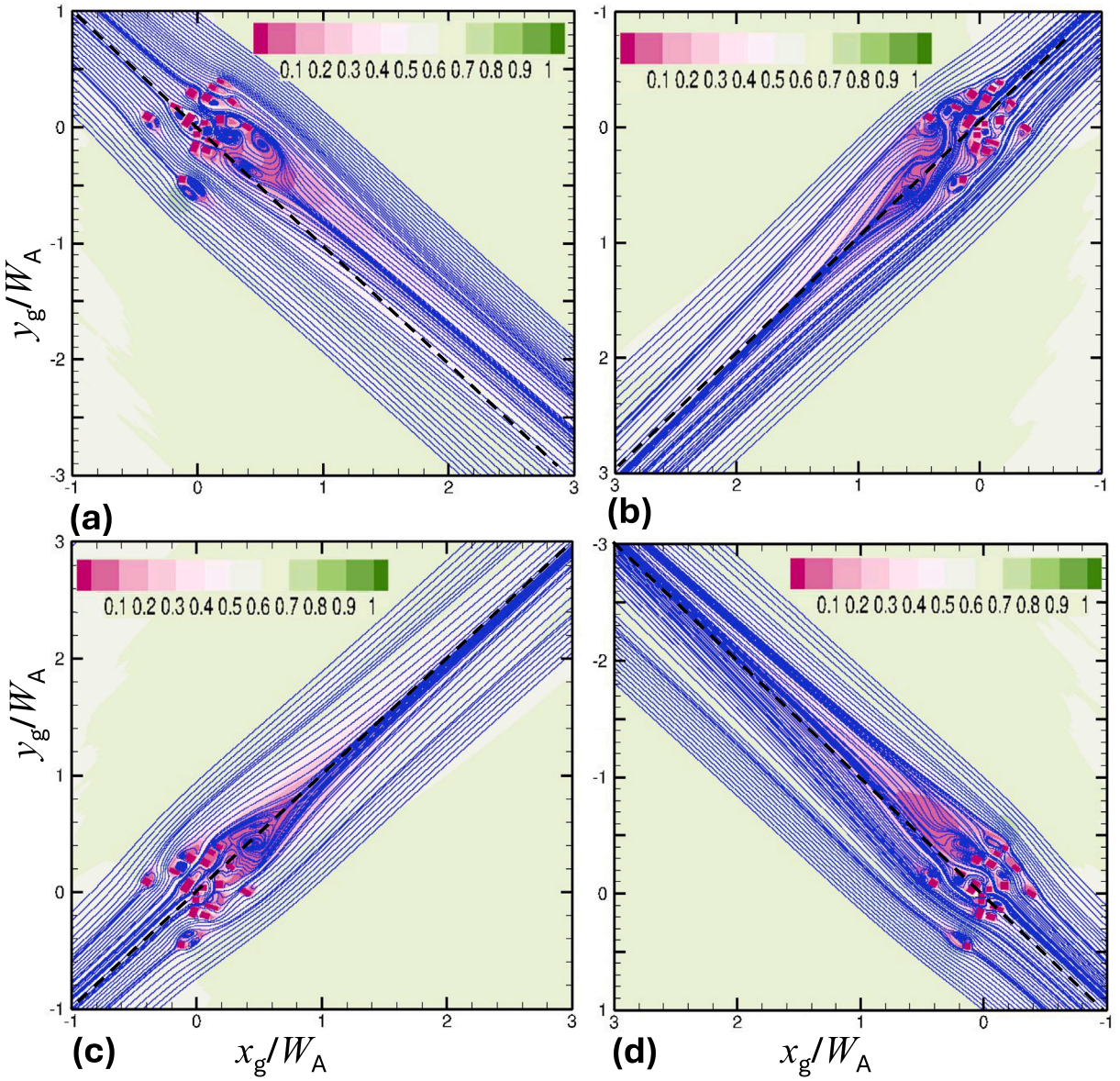

Fig. 12. Contours of time-averaged velocity normailized by freestream velocity U_∞ and streamlines generated from the horizontal time-averaged velocities at half average building height ($z/H_{ave} = 0.5$) for (a) NW, (b) NE, (c) SW, and (d) SE winds, with along-wind cluster centreline indicated (dashed lines).

Fig. 12d, where no primary recirculation is evident at the same height. The tallest and widest cuboid-shaped building, B5, with a height of $1.9H_{\text{ave}}$, is positioned across the cluster centreline with its long horizontal edge nearly perpendicular to the NW and SE wind directions (Fig. 5), resulting in a distinct secondary recirculation on its upper leeward side (Fig. 12d).

The wake under NE wind conditions (Fig. 12d) exhibits a distinct low-speed zone but lacks a clear primary recirculation, likely due to the asymmetric and complex recirculation pattern shown in Fig. 12b. In contrast, the wake under SW wind conditions displays a flow pattern similar to that of a single tall building, such as the CAARC building (Daniels et al., 2013). An elevated primary recirculation region is evident in Fig. 12b, with a saddle point at $z/H_{\text{ave}} = 0.8$ separating a secondary recirculation at $z/H_{\text{ave}} = 1$ from the primary one. This confirms the SW wind case experiences the greatest cluster solidity (Fig. 6). It should be noted that the wake flows are highly three-dimensional, making interpretation from horizontal and vertical planes challenging.

To better understand where the wake core occurs, the velocity deficit is calculated,

$$U_d(x,\ y,\ z) = U_0(x,\ y_0,\ z) - U(x,\ y,\ z), \tag{12}$$

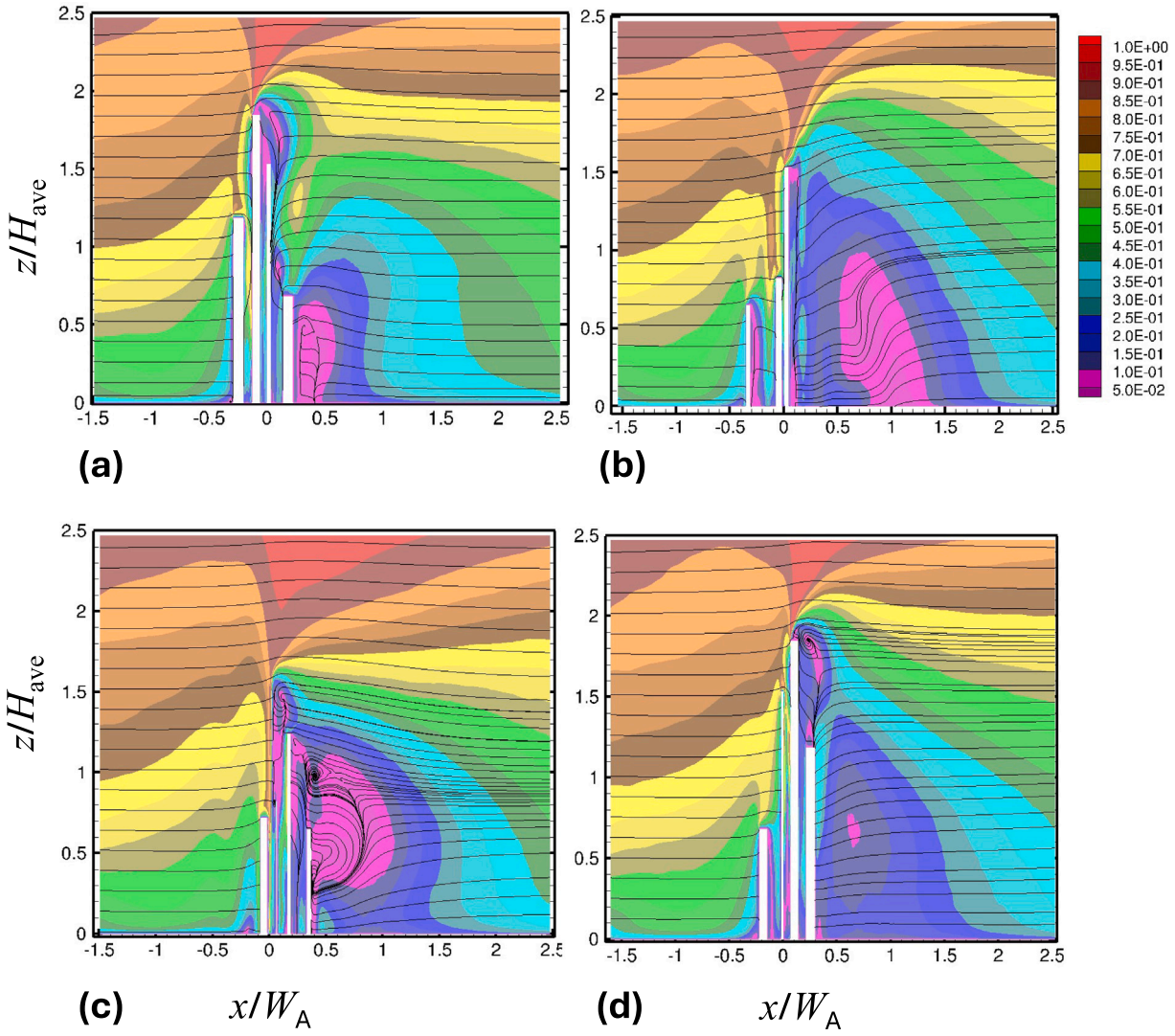

Fig. 13. As Fig. 12, but on a vertical along-wind cluster centreplane ($y = 0$).

where U_0 is the undisturbed streamwise velocity at (x, y_0, z) - far from the cluster and wake region. Fig. 14 presents horizontal profiles of the normalised mean streamwise velocity deficit U_d/U_0 at $z = 0.5H_{ave}$ for the SW, SE, NE and NW winds. The peaks of the velocity deficit for the SW and NE winds are aligned with the cluster centreline (Fig. 14a,c), whereas for the SE and NW winds the peaks are displaced off the cluster centreline (Fig. 14b,d), consistent with the wake behaviour observed in Fig. 12. For the SE wind, the deviation angle is approximately −1.3°. However, during a NW wind, two separate wakes occur. The velocity deficit profiles are clear (Fig. 14d), with the deviation from the centreline (based on peak velocity deficit locations between $x/W_A = 0.7$ and 4.0) is approximately 6.1° for the B4 wake (purple dashed line) and −3.7° for the wake generated by the remaining buildings (red dashed line).

Estimating the centre location and size of a wake velocity deficit profile or a scalar plume is not trivial when the profile deviates from a perfect Gaussian shape. The difficulty arises from distribution complexity, particularly in the near field. One approach to estimating the spread of a wake/plume uses:

$$\beta = \frac{\int_{-\infty}^{\infty} y\psi(y)\,dy}{\int_{-\infty}^{\infty} \psi(y)\,dy}, \tag{13}$$

where β is the local coordinate of the plume centre, ψ is the wake velocity deficit or the concentration at the local coordinate y. The half-plume width σ, representing the standard deviation, is calculated using:

$$\sigma^2 = \frac{\int_{-\infty}^{\infty} (y-\beta)^2\psi(y)\,dy}{\int_{-\infty}^{\infty} \psi(y)\,dy}. \tag{14}$$

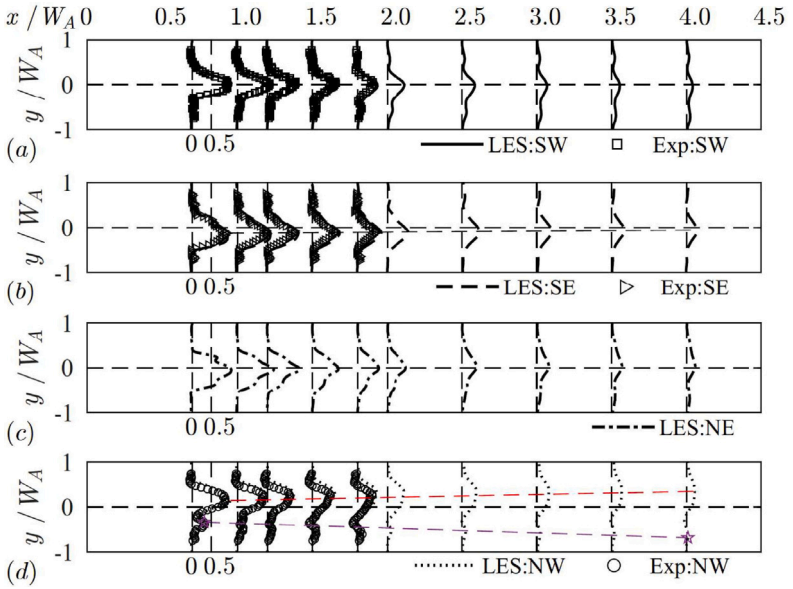

Fig. 14. Normalised mean streamwise velocity deficit (U_d/U_0, Eq. (12)) at $z = 0.5H_{ave}$ from LES (lines) and wind tunnel (Exp., circles) data for different wind directions: (a) SW, (b) SE (deviation angle $\alpha = -1.3°$), (c) NE and (d) NW (Deviation angles $\alpha = -3.7°$ for main cluster, and 6.1° for secondary cluster).

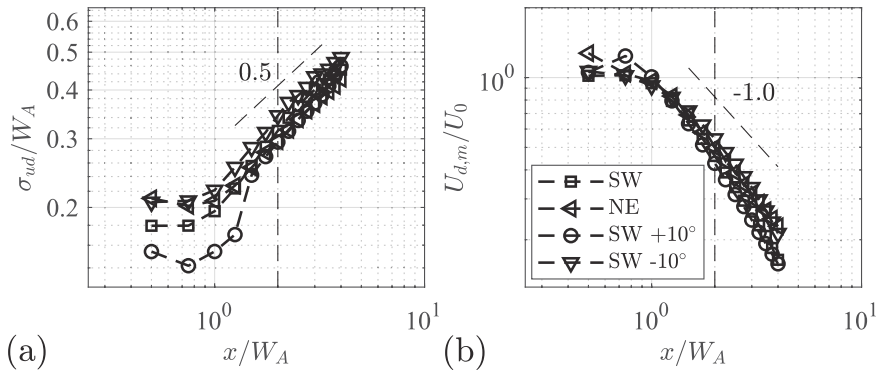

Fig. 15. Normalised wake properties at z/H_{ave} = 0.5 m generated from the LES data for four wind directions (SW ± 10°, NE) : (a) horizontal wake width (σ_{ud}) and (b) and peak velocity deficit ($U_{d,m}$).

For a horizontal profile Eqs. (13)–(14) are integrated from $-\infty$ to $+\infty$. For vertical profiles, the data are processed by, (1) creating a symmetric distribution about the ground by mirroring the profile above the ground plane, and (2) entire profile is integrated from $-\infty$ to $+\infty$ in the vertical direction to calculate σ.

Given with SW and NE winds the wakes have a clearly merged structure (cf. other directions, Fig. 12), we analyse the wake width and peak velocity deficit for the SW ± 10° and NE directions (Fig. 15). In the far field ($x \geq 1.5W_A$ downstream of the cluster centre) the four σ_{ud}/W_A profiles collectively increase as $(x/W_A)^{0.5}$ (Fig. 15a), while their peak velocity deficit $U_{d,m}/U_0$ profiles decrease as $(x/W_A)^{-1.0}$ (Fig. 15b). The former is consistent with Eames et al. (2011)'s investigation of a circular cylinder in ambient turbulence, with the wake to grow diffusively (i.e. proportional to $x^{0.5}$ when its width is larger than the flow integral length scale). Exponents in the range of 0.5 to 1.0 are typically associated with far-field diffusion under homogeneous conditions

4.2. Spatially averaged turbulent stresses and dispersive stresses

To examine the turbulence statistics within and above the CoL cluster area (700 m in diameter, Fig. 5), spatial averaging velocity component are decomposed:

$$u_i(x, y, z, t) = \langle U_i \rangle(z) + \tilde{u}_i(x, y, z) + u_i'(x, y, z, t), \tag{15}$$

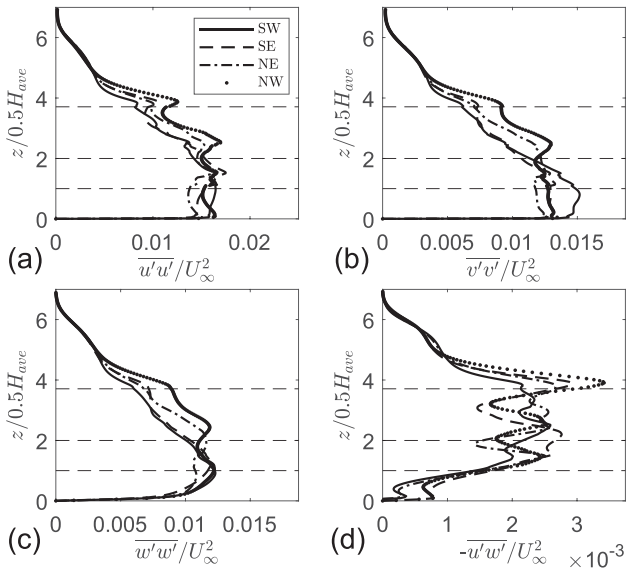

Fig. 16. Dimensionless spatially-averaged turbulent normal stresses (a) $\overline{u'u'}/U_\infty^2$, (b) $\overline{v'v'}/U_\infty^2$, (c) $\overline{w'w'}/U_\infty^2$, and (d) turbulent shear stress $-\overline{u'w'}/U_\infty^2$ when the wind is from four directions(SW, SE, NE, and NW).

where $\langle U_i \rangle$ is horizontally averaged mean velocity, $\tilde{u}_i = U_i - \langle U_i \rangle$ is the spatial fluctuation of the mean flow (in time) and $u_i' = u_i - \langle U_i \rangle - \tilde{u}_i$ is the turbulent fluctuation, with the capital letter denoting a time average and angle brackets a horizontal spatial average for the CoL cluster area (Fig. 5). For this comprehensive spatial averaging (e.g. Xie and Fuka, 2018) the building volume, with a zero velocity, is taken into account in the average. $\langle \tilde{u}\tilde{u} \rangle$, $\langle \tilde{v}\tilde{v} \rangle$, and $\langle \tilde{w}\tilde{w} \rangle$ are customarily referred to as the dispersive normal stresses, while $\langle \tilde{u}\tilde{w} \rangle$ is the dispersive shear stress (Raupach and Shaw, 1982; Finnigan, 2000). By definition, dispersive stresses arise from spatial inhomogeneities in the time-averaged velocities (e.g. Coceal et al., 2006; Xie et al., 2008).

Surprisingly, the turbulent normal stresses ($\overline{u'u'}$, $\overline{v'v'}$ and $\overline{w'w'}$) are largely insensitive to wind directions both within and above the CoL cluster (Fig. 16a–c). Specifically, $\overline{u'u'}$ and $\overline{v'v'}$ are almost constant below $z = H_{ave}$ and then decrease above $z = H_{ave}$, while $\overline{w'w'}$ peaks below H_{ave} and then decreases. The turbulent shear stress (Fig. 16d) $|\overline{u'w'}|$ peaks near $z = H_{ave}$ and then remains almost constant throughout the canopy. Above that, $|\overline{u'w'}|$ starts to decay rapidly, as expected. Small changes in wind directions (SW ± 10°) suggest the turbulent stresses are insensitive, at least in neutral conditions with largely invariant wind directions (Fig. 2). This may have benefits when undertaking numerical modelling full-scale boundary layers over many hours. This insensitivity may be attributed to the mixing of turbulent fluctuations coupled with their stochastic nature.

On the other hand, the vertical profiles of dispersive normal and shear stress vary between different wind directions, with SW and NW directions having the larger dispersive shear stresses (Fig. 17). Above the tallest building, both normal and shear dispersive stresses decay rapidly. The dispersive stresses differ between directions on the same axis (e.g. SW→NE vs. NE→SW), despite having the same solidity in this cluster. For the SW conditions, $-\langle \tilde{u}\tilde{w} \rangle$ first increases, peaking below H_{ave} and then decreases rapidly to cluster canopy top. The same trend occurs for SW dispersive normal stresses with different peak locations. However, for the NE there are large differences, such as location of the peak, and variations below and above this for both dispersive normal and shear stresses. A building-height step change exists (SW experiencing a step-up, NE a step-down, Fig. 5) may cause these differences in the dispersive stress profiles. A further wind direction (SW ± 10°) sensitivity test for dispersive stresses indicates they are relatively insensitive within this range of directions, suggesting the mean flow geometry does not change significantly within this SW range.

4.3. Dispersion upstream and within cluster wake

When the flow is from the NW, with a ground-level release (Fig. 18), the ground-level plume spreads abruptly, flowing both around the building cluster (e.g. B13, B14, and B15, Fig. 5) and in the channels between the buildings (Fig. 18a). This results in high- and low-concentration areas within the horizontal plane. A vertical cross-section at $y = 0$ (Fig. 18b) shows consistent concentrations (cf. 18a), with the plume spreading rapidly as the cluster blockage is encountered. Downstream of the cluster, the plume spread is much slower (Fig. 18b). The tracer experiences rapid vertical transport in the near wake of the buildings, consistent with Pascheke et al. (2008)'s shorter building case and Bi et al. (2024)'s idealised, regular square cross-section tall building cluster. This 'bimodality of the plume' (Bi et al., 2024) has buildings beyond the tallest building being fully engulfed by the plume, with smaller vertical concentration gradients (cf. upstream), indicating rapid mixing downwind of the tallest building.

A fraction of the mean flow passes through the cluster while the remainder is deflected over and around it, with the dominating process depending on local geometry. Flow passing through the cluster continues to decelerate, driving secondary flow upwards and

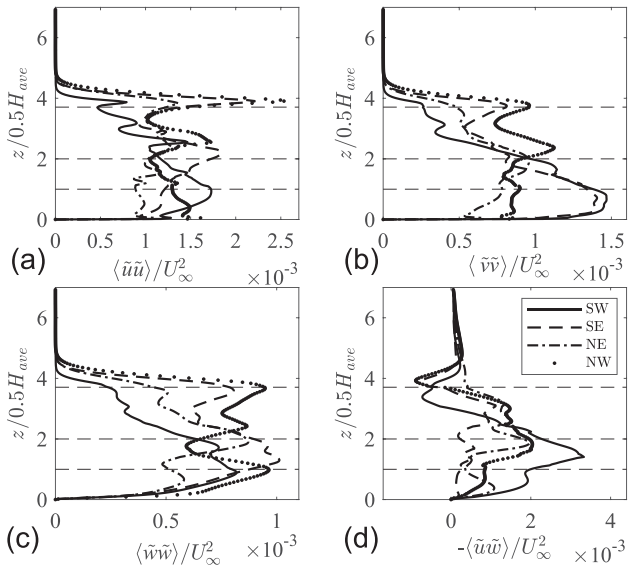

Fig. 17. Dimensionless spatially-averaged dispersive normal stresses (a) $\langle\tilde{u}\tilde{u}\rangle$, (b) $\langle\tilde{v}\tilde{v}\rangle$, (c) $\langle\tilde{w}\tilde{w}\rangle$, and (d) dispersive shear stress $\langle\tilde{u}\tilde{w}\rangle$ for four wind directions (SW, SE, NE, and NW).

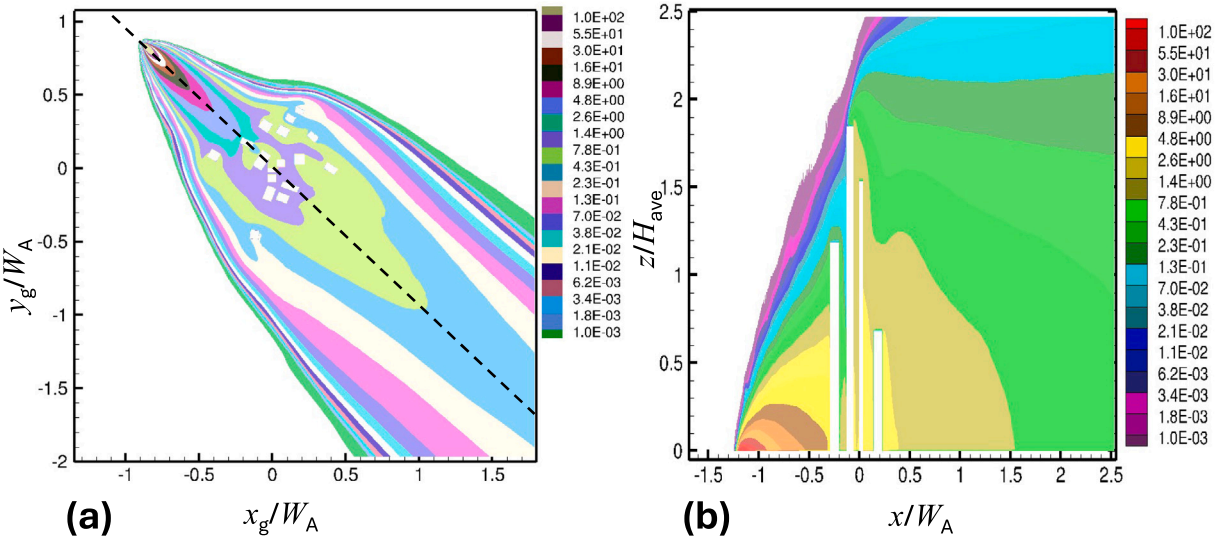

Fig. 18. Dimensionless concentration C^* (colour bar) of a source released at ($x = -1.25W_A, y = 0$, and $z = 0$) in NW wind, showing (a) a horizontal plane at $z = 0$, (b) a vertical plane at $y = 0$.

outwards, and advecting scalar with it. As a consequence of the vertical spreading in the building near wakes and the topographically driven lateral dispersion, the plume leaving the cluster has dimensions determined by the cluster geometry as a whole (height and width), as well as the source location. In detail, the flow becomes a combination of jets and wakes that coalesce in the near-wake of the cluster and dictate the flow field locally. Wake recovery is a slower process than occurs upstream in the perturbed flow.

The lateral plume dispersion within the cluster is similar to that of other arrays of obstacles (Fig. 18). The lateral spread extent depends on the geometry, with building spacing controlling if there is sufficient space for the scalar to spread into adjacent near-wakes and, hence, across the array. Although more complicated in an irregular array, the processes remain largely the same. Notable differences in lateral spread are largely immediately downwind of the cluster. This could be considered as a virtual source origin upwind of the actual location. The concept of a virtual origin is well established (e.g. Boppana et al., 2012). A point-source plume passing around an obstacle experiences enhanced spreading. Far downstream of the obstacle, the plume width can be estimated by fitting its spread to a Gaussian profile. By extrapolating the curve of plume width versus downstream distance (e.g. Fig. 20), the

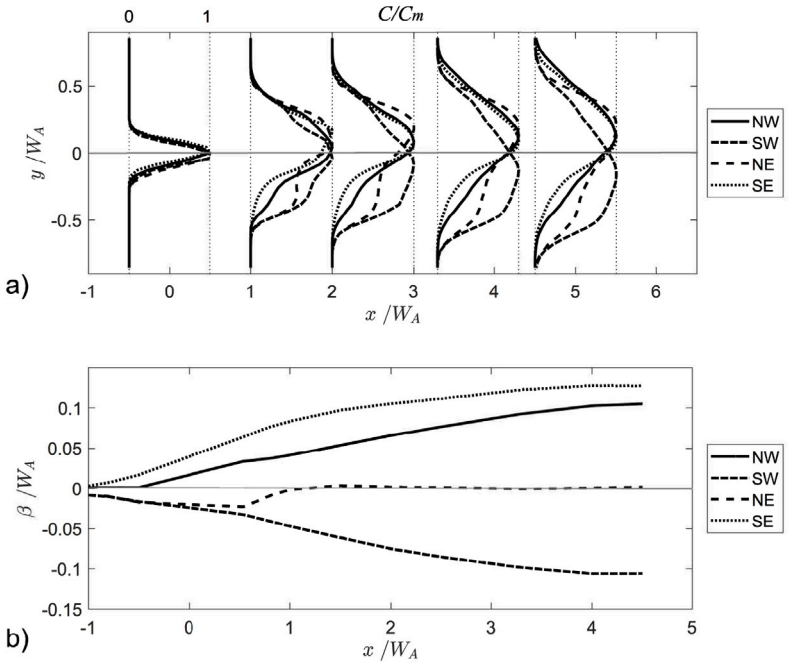

Fig. 19. For four wind directions (NW, SW, NE, and SE), (a) the mean concentration normalised by the respective maximum local mean concentration at $x/W_A = -0.5$, 1, 2, 3.3 and 4.5, and $z = 0$, and (b) the plume centre coordinates β.

location where the plume width approaches zero — the virtual source — can be determined. Thus, the effective distance x_s can be much greater.

As possibly expected, lateral ground-level profiles of dimensionless mean concentration upwind of the building cluster appear Gaussian-like, with a centreline deviating from the wind direction as it approaches the cluster (see Fig. 19a). Obviously, these characteristics depend on specific source location (i.e., varying if nearer/further from the cluster), but we expect the trend around the cluster to be general. Immediately downstream of the cluster, the plume has considerably spread horizontally, as expected. Thereafter, the plume symmetry breaks linked to the cluster's asymmetric spatial variability, with the centre shifted from the along-wind centreline (Fig. 19a).

The concentration profiles are used to determine the plume centreline position (β, Eq. (13), e.g. cross-wind, Fig. 19b), as well as the half lateral and vertical plume widths (σ_y and σ_z, respectively, Eq. (14)). Given the inflow turbulence lateral integral length scale $L_y \ll 2\sigma$ and the plume size $2\sigma \approx W_A$ (cluster size), one would expect that turbulent convection may be weak and the plume-centre shift to be largely controlled by the dynamics of the cluster wake. The shift is in a positive y direction ($\beta > 0$) for the NW and SE winds (Fig. 20), consistent with the wake shift (Fig. 12).

For the SW case, with the maximum solidity (Fig. 6) and most concentrated wake (Fig. 12), the plume more abruptly spreads with flow around the cluster rather than penetrating into it. This can cause the plume centre to shift to either side of the cluster, resulting in a large deviation of the plume centreline from the wake centre (Fig. 19), whereas, the wake for the NE flow has the widest spread (Fig. 12), with $\beta \approx 0$ in the farfield. The cluster wake flow (Section 4.1.2) behaves very differently in the SW and NE winds, attributed to the inhomogeneous building layout. Although corridors exist for the flow and scalar to pass, the heterogeneous building layout, sizes and orientations make the cluster scalar dispersion differ considerably for these two directions.

Distinctly different plume spread behaviour occurs upwind and downwind of the cluster (Figs. 19–20). Upwind, both σ_y and σ_z vary initially as $x_s^{1.0}$, then slightly more rapidly as the cluster is approached. The peak concentration decays as $x_s^{-1.5}$, right up to the cluster. The plume spread is much slower downwind of the cluster, varying as $x_s^{0.5}$, and the peak concentration decays as $x_s^{-1.0}$. These results seem consistent. However, we should note the choice of origin is entirely arbitrary, so possibly fortuitous if this is an optimum to describe plume development. Much of the plume spread variation must reflect the slow development of a highly irregular profile just downwind of the cluster to a more regular form further downstream. A very long fetch may be necessary to reach a theoretical Gaussian form. The large centreline offsets we see (Fig. 19) are consistent with this.

As noted, the peak lateral location may deviate from the cluster centreline. We analyse the normalised vertical profiles with lateral offsets (Fig. 21a) for two locations downstream of the cluster. There is clearly some spread between the individual profiles, which is mainly due to the different wind directions, again highlighting the cluster's heterogeneity influence on dispersion. For one direction (SW, Fig. 21b) the profiles are shown for two locations upstream and four downstream of the cluster. Without the cluster, we would expect the upstream profiles to collapse to a single curve. Thus, it is clear the cluster is significantly influencing the upstream fetch conditions by creating a blockage. Downstream of the cluster, the profiles overlap somewhat, suggesting partial recovery of the plume structure.

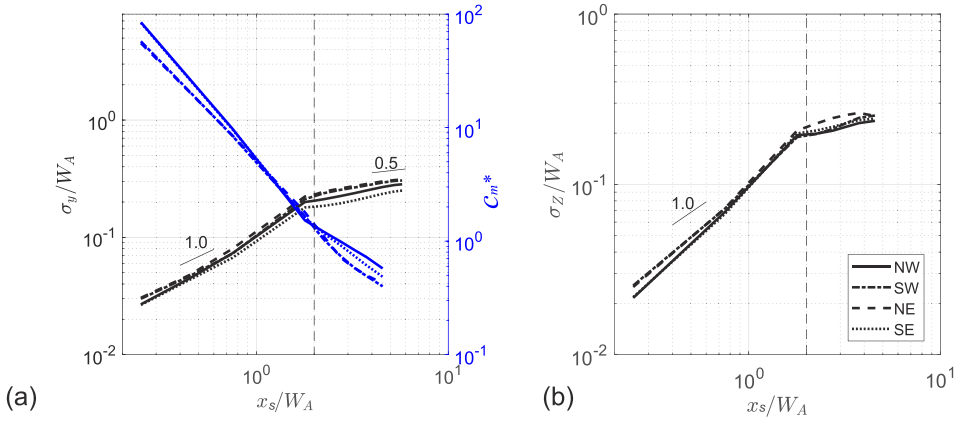

Fig. 20. Plume characteristics for four wind directions (NW, SW, NE and SE) showing (a) horizontal half-width σ_y and peak concentration C_m^* at $z = 0$, and (b) vertical width σ_z on the along-wind vertical plane with the local ground-level peak concentration identified. The origin (x_s, y_s, z_s) is at the source location ($x_s = x + 1.25W_A$, $y_s = y$, $z_s = z$) with the building cluster centre (dashed line) shown.

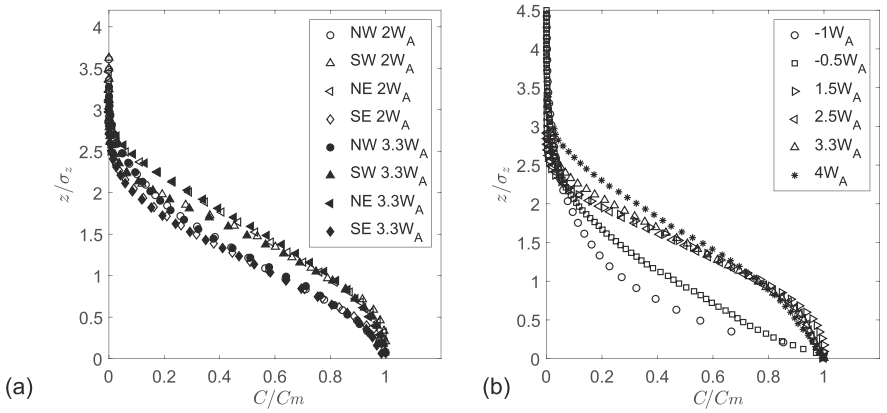

Fig. 21. For different wind directions (NW, SW, NE and SE) the normalised vertical profiles (by σ_z) of mean concentration (by peak ground-level concentration C_m) at (a) $x/W_A = 2$ and 3.3, and (b) $x/W_A = -1$, -0.5, 1.5, 2.5, 3.3 and 4 (SW wind).

5. Summary and discussions

We were able to identify a day with a nearly neutral and stationary urban boundary-layer flow. Therefore, caution must be exercised when interpreting these data. Castro et al. (2006) observed in wind-tunnel experiments that the integral length scale immediately above an array of cubes is of the same order of magnitude as the cube size. The BT Tower height is approximately ten times the average upstream building height of about 20 m (Xie and Castro, 2009), and the integral length scale at this elevation is likely influenced not only by the building size but also by additional factors. MacGarry et al. (2025) further showed, using large-eddy simulations, that the integral length scale above and downstream of a large array of tall buildings is significantly affected by the building height. From the BT Tower measurements, a non-dimensional peak frequency of $n_p = 0.14$ was obtained. This corresponds to an integral length scale of $L_x \approx 200$ m, which is an order of magnitude greater than the average upstream building height.

By using wavelet analysis, we identified a dominant vortex-shedding frequency associated with the cluster of tall buildings under southwesterly winds. Its corresponding dimensionless frequency — the Strouhal number — was found to be approximately 0.14 when based on an effective cluster width W_e, a value close to that of a single square cylinder. Both numerical (Nguyen et al., 2023) and experimental (Mishra et al., 2024) studies of regular building arrays have shown that the dominant vortex-shedding frequency is governed by the cluster scale rather than by the size of individual buildings, further confirming the cluster effect on vortex shedding. MacGarry et al. (2025) performed LES using a domain with the same ratio of boundary-layer thickness to average building height for a very large array, and reported that no dominant vortex shedding was observed. This supports the conclusion that the dominant vortex identified in the present study is not caused by oscillations of the boundary-layer height.

Mean-flow visualisation reveals a clear wake-merging phenomenon downstream of the near field. In particular, for southwesterly winds, the wake at half the average building height exhibits a single, attached large-scale recirculation region and a consolidated wake downstream. For southeasterly winds, however, the wakes generated by individual buildings do not fully merge into a

single wake until near the outlet of the 4 km computational domain. This indicates that the wake-merging process depends on the effective cluster solidity, which varies with wind direction. Both experimental studies (Mishra et al., 2023, 2024) and LES investigations (Nguyen et al., 2023; Inam et al., 2026) of regular arrays of tall buildings demonstrate that smaller wakes shed by individual buildings ultimately merge to form a larger, unified wake structure.

The scalar concentration contours exhibit a clear step change in both the horizontal and vertical directions, caused by the flow perturbations induced by the building cluster. Wind-tunnel studies on regular arrays of buildings have reported similar behaviour. Mishra et al. (2024) showed that the horizontal growth of the wake evolves in a complex manner, particularly within the near-wake and transition regions. Mishra et al. (2023) further demonstrated that, in the near-wake region, the decay of the centreline velocity deficit behind a cluster of buildings is similar to that behind a single building when scaled with the size of the individual buildings. Bi et al. (2025) showed an increase in the pollutant concentration behind the buildings, essentially due to the capturing of the pollutant in their wake. This behaviour supports the deviation of the peak concentration location along the direction of the wake, as observed for different wind directions in the present case. Additionally, they observed that the plume boundary for an upstream-located source case showed a contraction–expansion pattern due to lateral channelling and cluster-scale recirculation, which further supports the characteristics of the wake width plotted in Fig. 15 of the present manuscript.

6. Concluding remarks

Through undertaking both scaled (1:500) laboratory experiments and full-scale large-eddy simulations (LES), we study the flow and dispersion fields around and within a cluster (a group) of 17 geometrically simplified tall buildings, representative of the City of London. We analyse four different wind directions (NW, NE, SW, and SE). Field observations at 191 m above ground level on one day (12 March 2020) are used to inform dynamic similarity analysis for the laboratory and the LES, when near-neutral conditions occur within the urban boundary layer over London. The full-scale integral time and length scale (L_x) are found to be approximately 2 min and 200 m, respectively (when the mean wind speed is $\approx$14 ms^{-1}), broadly consistent with previously studies (Wood et al., 2009; Lean et al., 2019; Theeuwes et al., 2025). After successfully evaluating the LES using laboratory mean to second-order moment statistics for both velocity and concentration fields, we analyse our LES model runs.

For the wind directions simulated, different wake deflections are generated, with complex flow features spanning from single to multilobed wake profiles. In the near field, the general flow dynamics strongly depend on the interplay and merging of individual wakes generated by each cluster building and its spacing. In the far field, the wake width increases as $(x/W_A)^{0.5}$, while peak velocity deficit decreases as $(x/W_A)^{-1.0}$. A Strouhal number of $St = 0.136$, is obtained based on the dominant vortex shedding frequency, the effective cluster width and the freestream velocity, as identified in sampled far wake velocity under SW conditions. These wake and vortex shedding characteristics indicate a pronounced clustering effect of the 17 tall buildings, despite the cluster's relatively low packing density of $\lambda_p \approx 9\%$.

Equally important are the spatially-averaged turbulent stresses over the cluster area. These are insensitive to direction across those considered (i.e. NW, NE, SW, and SE) both within and above the CoL cluster. Whereas, the dispersive stresses over the cluster area exhibit substantial variations between wind directions, even when encountering the same cluster solidity (i.e. wind blowing in opposite directions). These findings span wake development, dominant vortex shedding frequency, spatially averaged turbulent stresses, and dispersive stresses, hence, with important implications when addressing central business districts (CBDs), to advance wind engineering, microclimate modelling and/or O(100 m)-resolution meso-scale numerical weather prediction (NWP).

To assess the effects of a tall building cluster of a ground-level passive scalar release immediately upwind of the cluster, both laboratory and LES data are analysed. The vertical plume has distinct regions that differ between upwind and downwind of the cluster. Upstream, the plume spread is rapid with the vertical width growing faster than $\sigma_z \sim x_s^{1.0}$, because of the cluster created blockage. Downstream, the spread is notably slower with $\sigma_z \sim x_s^{0.5}$, attributed to the enhanced vertical scalar transport in the buildings' near wakes.

Laterally, the plume transport is sensitive to building orientation within the cluster relative to wind direction (i.e., exact building layout). While the plume concentration is near Gaussian, its centre may shift away from the cluster's along-wind centreline for some wind directions (i.e., controlled by within-cluster building alignment). These large shifts of plume centre from the cluster's along-wind centreline can persist, seen here for our entire downwind domain (i.e. $4.5W_A$). Similarly to vertical spreading, when the plume approaches the cluster, its lateral spread is enhanced, with its lateral width growing faster than $\sigma_y \sim x_s^{1.0}$, notably for the highest solidity (i.e. here for SW), forcing the plume to advect around rather than penetrating the cluster. This causes the large plume-centre deflections from the cluster's along-wind centreline. The irregular cluster of the 17 tall buildings is characterised by a very large vertical and lateral spread immediately downwind of the cluster, providing a source virtual origin much upwind of its actual location for Gaussian dispersion models (e.g. ADMS, Carruthers et al., 1999).

This work documents our efforts to characterise the temporal and spatial scales of the incoming urban boundary layer, as well as the turbulent flow and scalar fields around real-world clusters of tall buildings, and their sensitivity to variations in urban wind direction. Ensuring that such analyses are extensible beyond the limited set of available case studies is of crucial importance, yet remains highly challenging. For example, Nazarian et al. (2025) simulated 538 urban layouts using large-eddy simulations to create an open-access database for urban canopy-layer parameterisation, highlighting both the diversity of possible configurations and the difficulty of generalising across them. Nevertheless, we have attempted to compare the behaviour of real-world clusters of tall buildings with that observed in various regular arrays of square cross-section tall buildings, with the aim of identifying common underlying characteristics. We hope that these findings help clarify which aspects of the flow can be generalised — and therefore potentially modelled — and which remain inherently site-specific.

CRediT authorship contribution statement

Changchang Wang: Writing – original draft, Visualization, Validation, Methodology, Investigation, Formal analysis. **Abhishek Mishra:** Writing – original draft, Methodology, Investigation, Formal analysis. **Dominic Clements:** Writing – original draft, Visualization, Methodology, Investigation, Formal analysis. **Dianfang Bi:** Writing – review & editing, Methodology, Investigation, Formal analysis. **Marco Placidi:** Writing – review & editing, Supervision, Resources, Project administration, Methodology, Funding acquisition, Data curation, Conceptualization. **Davide Lasagna:** Supervision, Methodology, Funding acquisition, Formal analysis. **Omduth Coceal:** Writing – review & editing, Supervision, Funding acquisition. **Janet Barlow:** Writing – review & editing, Supervision, Methodology, Funding acquisition, Conceptualization. **Matteo Carpentieri:** Writing – review & editing, Supervision, Methodology, Funding acquisition, Conceptualization. **Sue Grimmond:** Writing – review & editing, Supervision, Funding acquisition, Conceptualization. **Alan Robins:** Writing – review & editing, Supervision, Funding acquisition, Conceptualization. **Zheng-Tong Xie:** Writing – review & editing, Supervision, Software, Resources, Methodology, Funding acquisition, Data curation, Conceptualization.

Funding

This research was supported by EPSRC, United Kingdom under the agreement (EP/V010921/1, EP/V010166/1, EP/V010514/1), titled 'Fluid dynamics of Urban Tall-building clUsters for Resilient built Environments (FUTURE)' coordinated by the University of Surrey.

Declaration of competing interest

The authors declare that they have no known competing financial interests or personal relationships that could have appeared to influence the work reported in this paper.

Acknowledgements

The computations were performed on the National Supercomputing System ARCHER2 and the IRIDIS 5 supercomputer facility at the University of Southampton. We are grateful to Dr Saad Inam for carrying out some initial LES simulations.

Data availability

Data will be made available on request.

References

Allwine, K.J., Shinn, J.H., Streit, G.E., Clawson, K.L., Brown, M., 2002. Overview of URBAN 2000: A multiscale field study of dispersion through an urban environment. Bull. Am. Meteorol. Soc. 83 (4), 521–536.

Arnold, S., ApSimon, H., Barlow, J., Belcher, S., Bell, M., Boddy, J., Britter, R., Cheng, H., Clark, R., Colvile, R., et al., 2004. Introduction to the DAPPLE air pollution project. Sci. Total Environ. 332 (1–3), 139–153.

Auerswald, T., Klippel, K., Thomas, T.G., Goulart, E.V., Carpentieri, M., Hayden, P., Hertwig, D., Reis, N.C., Robins, A., Coceal, O., 2024. Effect of flow variability on dispersion of continuous and puff releases in a regular street network. Bound.-Layer Meteorol. 190 (4), 20. http://dx.doi.org/10.1007/s10546-024-00863-z.

Ayet, A., Katul, G., 2020. Scaling laws for the length scale of energy-containing eddies in a sheared and thermally stratified atmospheric surface layer. Geophys. Res. Lett. 47 (23), e2020GL089997.

Barlow, J., 2014. Progress in observing and modelling the urban boundary layer. Urban Clim. 10, 216–240.

Barlow, J.F., Dunbar, T., Nemitz, E., Wood, C.R., Gallagher, M., Davies, F., O'Connor, E., Harrison, R., 2011. Boundary layer dynamics over London, UK, as observed using Doppler lidar during REPARTEE-II. Atmospheric Chem. Phys. 11 (5), 2111–2125.

Bearman, P., Morel, T., 1983. Effect of free stream turbulence on the flow around bluff bodies. Prog. Aerosp. Sci. 20 (2–3), 97–123.

Bearman, P., Obasaju, E., 1982. An experimental study of pressure fluctuations on fixed and oscillating square-section cylinders. J. Fluid Mech. 119, 297–321.

Bi, D., Mishra, A., Placidi, M., Robins, A., Carpentieri, M., 2024. Pollutant dispersion and bimodality in tall building clusters. In: 14th UK Conference on Wind Engineering. Southampton, http://dx.doi.org/10.5258/WES/P0055.

Bi, D., Mishra, A., Placidi, M., Robins, A., Carpentieri, M., 2025. Wind tunnel study of source location effects on pollutant dispersion around uniform tall building clusters. J. Wind Eng. Ind. Aerodyn. 266, 106194.

Boppana, V.B.L., Xie, Z.-T., Castro, I.P., 2012. Large-eddy simulation of dispersion from line sources in a turbulent channel flow. Flow, Turbul. Combust. 88 (3), 311–342.

Braun, A.L., Awruch, A.M., 2009. Aerodynamic and aeroelastic analyses on the CAARC standard tall building model using numerical simulation. Comput. Struct. 87 (9), 564–581. http://dx.doi.org/10.1016/j.compstruc.2009.02.002, URL: https://www.sciencedirect.com/science/article/pii/S0045794909000376.

Breuer, M., Bernsdorf, J., Zeiser, T., Durst, F., 2000. Accurate computations of the laminar flow past a square cylinder based on two different methods: lattice-Boltzmann and finite-volume. Int. J. Heat Fluid Flow 21 (2), 186–196.

Brixey, L.A., Heist, D.K., Richmond-Bryant, J., Bowker, G.E., Perry, S.G., Wiener, R.W., 2009. The effect of a tall tower on flow and dispersion through a model urban neighborhood Part 2. Pollutant dispersion. JEM 11 (12), 2171–2179. http://dx.doi.org/10.1039/b907137g.

Burian, S.J., Maddula, S.R.K., Velugubantla, S.P., Brown, M.J., 2002. Morphological Analyses Using 3D Building Databases: Albuquerque, New Mexico. Technical Report. LA-UR-02-6198, LA-UR-02-6198, Los Alamos National Laboratory, Los Alamos, New Mexico.

Carruthers, D., McKeown, A., Hall, D., Porter, S., 1999. Validation of ADMS against wind tunnel data of dispersion from chemical warehouse fires. Atmos. Environ. 33 (12), 1937–1953.

Castro, I.P., Cheng, H., Reynolds, R., 2006. Turbulence over urban-type roughness: deductions from wind-tunnel measurements. Bound.-Layer Meteorol. 118, 109–131.

Castro, I., Robins, A., 1977. The flow around a surface-mounted cube in uniform and turbulent streams. J. Fluid Mech. 79 (2), 307–335.
Castro, I.P., Xie, Z.-T., Fuka, V., Robins, A.G., Carpentieri, M., Hayden, P., Hertwig, D., Coceal, O., 2017. Measurements and computations of flow in an urban street system. Boundary-Layer Meteorol. 162 (2), 207–230.
Cezana, F.C., Goulart, E.V., Reis, N.C., Coceal, O., 2021. Analysis of pollutant entrainment from localized sources in a street network. Bound.-Layer Meteorol. 179 (2), 241–258. http://dx.doi.org/10.1007/s10546-020-00598-7.
Chen, Y., Djidjeli, K., Xie, Z.-T., 2020. Large eddy simulation of flow past stationary and oscillating square cylinders. J. Fluids Struct. 97, 103107.
Coceal, O., Goulart, E.V., Branford, S., Thomas, T.G., Belcher, S.E., 2014. Flow structure and near-field dispersion in arrays of building-like obstacles. J. Wind Eng. Ind. Aerodyn. 125, 52–68. http://dx.doi.org/10.1016/j.jweia.2013.11.013.
Coceal, O., Thomas, T., Castro, I., Belcher, S., 2006. Mean flow and turbulence statistics over groups of urban-like cubical obstacles. Boundary-Layer Meteorol. 121 (3), 491–519.
Council on Tall Buildings and Urban Habitat, 2019. CTBUH height criteria. URL: https://www.ctbuh.org/resource/height (Accessed: 02 December 2019).
Daniels, S.J., Castro, I.P., Xie, Z.-T., 2013. Peak loading and surface pressure fluctuations of a tall model building. J. Wind Eng. Ind. Aerodyn. 120, 19–28.
Deardorff, J.W., 1980. Stratocumulus-capped mixed layers derived from a three-dimensional model. Bound.-Layer Meteorol. 18, 495–527.
DESA, 2018. Revision of World Urbanization Prospects. Vol. 16, UN Department of Economic and Social Affairs.
Diederich, F.W., Drischler, J.A., 1957. Effect of Spanwise Variations in Gust Intensity on the Lift Due to Atmospheric Turbulence. Technical Report..
Drew, D.R., Barlow, J.F., Lane, S.E., 2013. Observations of wind speed profiles over greater London, UK, using a Doppler lidar. J. Wind Eng. Ind. Aerodyn. 121, 98–105.
Eames, I., Jonsson, C., Johnson, P., 2011. The growth of a cylinder wake in turbulent flow. J. Turbul. (12), N39.
Elshaer, A., Aboshosha, H., Bitsuamlak, G., Damatty, A.E., Dagnew, A., 2016. LES evaluation of wind-induced responses for an isolated and a surrounded tall building. Eng. Struct. 115, 179–195. http://dx.doi.org/10.1016/j.engstruct.2016.02.026, URL: https://www.sciencedirect.com/science/article/pii/S0141029616001140.
Eurocode, 2005, EN 1991-1-4, Eurocode 1: Actions on structures -Part 1-4: General actions -Wind actions, Volume EN 1991-1-4:2005+A1, doi:ICS 91.010.30;93.040.
Filioglou, M., Preissler, J., Troiville, A., Thobois, L., Vakkari, V., Auvinen, M., Fortelius, C., Gregow, E., Hämäläinen, K., Hellsten, A., et al., 2022. Evaluating modelled winds over an urban area using ground-based Doppler lidar observations. Meteorol. Appl. 29 (2), e2052.
Finnigan, J., 2000. Turbulence in plant canopies. Annu. Rev. Fluid Mech. 32 (1), 519–571.
Fuka, V., Xie, Z.-T., Castro, I.P., Hayden, P., Carpentieri, M., Robins, A.G., 2018. Scalar fluxes near a tall building in an aligned array of rectangular buildings. Boundary-Layer Meteorol. 167 (1), 53–76.
Goulart, E.V., Coceal, O., Branford, S., Thomas, T.G., Belcher, S.E., 2016. Spatial and temporal variability of the concentration field from localized releases in a regular building array. Bound.-Layer Meteorol. 159 (2), 241–257. http://dx.doi.org/10.1007/s10546-016-0126-0.
Goulart, E.V., Reis Jr., N., Lavor, V.F., Castro, I.P., Santos, J.M., Xie, Z.-T., 2019. Local and non-local effects of building arrangements on pollutant fluxes within the urban canopy. Build. Environ. 147, 23–34.
Grimmond, S., Ward, H.C., 2021. Urban measurements and their interpretation. In: Foken, T. (Ed.), Springer Handbook of Atmospheric Measurements. Springer International Publishing, Cham, pp. 1391–1423.
Han, B.-S., Park, S.-B., Baik, J.-J., Park, J., Kwak, K.-H., 2017. Large-eddy simulation of vortex streets and pollutant dispersion behind high-rise buildings. Q. J. R. Meteorol. Soc. 143 (708), 2714–2726.
Heist, D.K., Brixey, L.A., Richmond-Bryant, J., Bowker, G.E., Perry, S.G., Wiener, R.W., 2009. The effect of a tall tower on flow and dispersion through a model urban neighborhood Part 1. Flow characteristics. JEM 11 (12), 2163–2170. http://dx.doi.org/10.1039/b907135k.
Hertwig, D., Gough, H.L., Grimmond, S., Barlow, J.F., Kent, C.W., Lin, W.E., Robins, A.G., Hayden, P., 2019. Wake characteristics of tall buildings in a realistic urban canopy. Bound.-Layer Meteorol. 172 (2), 239–270.
Hertwig, D., Grimmond, S., Kotthaus, S., Vanderwel, C., Gough, H., Haeffelin, M., Robins, A., 2021. Variability of physical meteorology in urban areas at different scales: implications for air quality. Faraday Discuss. 226, 149–172.
Hertwig, D., Soulhac, L., Fuka, V., Auerswald, T., Carpentieri, M., Hayden, P., Robins, A., Xie, Z.-T., Coceal, O., 2018. Evaluation of fast atmospheric dispersion models in a regular street network. Environ. Fluid Mech. 18, 1007–1044.
Hutchins, N., Marusic, I., 2007. Evidence of very long meandering features in the logarithmic region of turbulent boundary layers. J. Fluid Mech. 579, 1–28.
Inam, S., Nguyen, C.H., Wang, C., Lasagna, D., Xie, Z.-T., 2026. Vortex shedding behind clusters of square cylinders. J. Hydrodyn. in press.
Kadasch, E., Sühring, M., Gronemeier, T., Raasch, S., 2021. Mesoscale nesting interface of the PALM model system 6.0. Geosci. Model. Dev. 14 (9), 5435–5465.
Kaimal, J.C., Finnigan, J.J., 1994. Atmospheric Boundary Layer Flows: Their Structure and Measurement. Oxford University Press.
Kaimal, J.C., Wyngaard, J., Izumi, Y., Coté, O., 1972. Spectral characteristics of surface-layer turbulence. Q. J. R. Meteorol. Soc. 98 (417), 563–589.
Kent, C.W., Grimmond, S., Barlow, J., Gatey, D., Kotthaus, S., Lindberg, F., Halios, C.H., 2017. Evaluation of urban local-scale aerodynamic parameters: implications for the vertical profile of wind speed and for source areas. Bound.-Layer Meteorol. 164 (2), 183–213.
Kim, Y., Castro, I.P., Xie, Z.-T., 2013. Divergence-free turbulence inflow conditions for large-eddy simulations with incompressible flow solvers. Comput. & Fluids 84, 56–68.
Kim, Y., Xie, Z.-T., Castro, I.P., 2011. A forward stepwise method of inflow generation for LES. In: Proceedings of the 6th International Conference on Fluid Dynamics. Vol. 1376, pp. 134–136.
Klein, M., Sadiki, A., Janicka, J., 2003. A digital filter based generation of inflow data for spatially developing direct numerical or large eddy simulations. J. Comput. Phys. 186 (2), 652–665.
Kotthaus, S., Grimmond, C.S.B., 2018. Atmospheric boundary-layer characteristics from ceilometer measurements. Part 2: Application to London's urban boundary layer. Q. J. R. Meteorol. Soc. 144 (714), 1511–1524.
Lean, H.W., Barlow, J.F., Halios, C.H., 2019. The impact of spin-up and resolution on the representation of a clear convective boundary layer over London in order 100 m grid-length versions of the met office unified model. Q. J. R. Meteorol. Soc. 145 (721), 1674–1689.
Leonard, B.P., 1979. A stable and accurate convective modelling procedure based on quadratic upstream interpolation. Comput. Methods Appl. Mech. Engrg. 19 (1), 59–98.
Lewalle, J., Ashpis, D.E., 2004. Estimation of time scales in unsteady flows in a turbomachinery rig, NASA/TM—2004–209452. Technical Report.
Lim, H.D., Hertwig, D., Grylls, T., Gough, H., Reeuwijk, M.v., Grimmond, S., Vanderwel, C., 2022. Pollutant dispersion by tall buildings: laboratory experiments and Large-Eddy Simulation. Exp. Fluids 63 (6), 92. http://dx.doi.org/10.1007/s00348-022-03439-0.
Lyn, D., Rodi, W., 1994. The flapping shear layer formed by flow separation from the forward corner of a square cylinder. J. Fluid Mech. 267, 353–376.
MacGarry, D., Vanderwel, C., Xie, Z.-T., 2025. Effects of aspect ratio on flow over arrays of tall buildings. J. Heat Fluid Flow 116, 109935.
Mahrt, L., 2009. Characteristics of submeso winds in the stable boundary layer. Bound.-Layer Meteorol. 130, 1–14.
Makedonas, A., Carpentieri, M., Placidi, M., 2021. Urban Boundary Layers Over Dense and Tall Canopies. Bound.-Layer Meteorol. 181 (1), 73–93. http://dx.doi.org/10.1007/s10546-021-00635-z, URL: https://link.springer.com/article/10.1007/s10546-021-00635-z.
Maronga, B., Gryschka, M., Heinze, R., Hoffmann, F., Kanani-Sühring, F., Keck, M., Ketelsen, K., Letzel, M.O., Sühring, M., Raasch, S., 2015. The parallelized large-eddy simulation model (PALM) version 4.0 for atmospheric and oceanic flows: model formulation, recent developments, and future perspectives. Geosci. Model. Dev. 8 (8), 2515–2551. http://dx.doi.org/10.5194/gmd-8-2515-2015, URL: https://gmd.copernicus.org/articles/8/2515/2015/.

Marucci, D., Carpentieri, M., 2019. Effect of local and upwind stratification on flow and dispersion inside and above a bi-dimensional street canyon. Build. Environ. 156, 74–88.
Marucci, D., Carpentieri, M., 2020. Dispersion in an array of buildings in stable and convective atmospheric conditions. Atmos. Environ. 222, 117100.
Marucci, D., Carpentieri, M., Hayden, P., 2018. On the simulation of thick non-neutral boundary layers for urban studies in a wind tunnel. Int. J. Heat Fluid Flow 72, 37–51.
Mason, P.J., Thomson, D.J., 1992. Stochastic backscatter in large-eddy simulations of boundary layers. J. Fluid Mech. 242, 51–78.
Mauder, M., Foken, T., Aubinet, M., Ibrom, A., 2021. Eddy-covariance measurements. In: Foken, T. (Ed.), Springer Handbook of Atmospheric Measurements. Springer International Publishing, Cham, pp. 1473–1504.
Melo, A., Santos, J., Reis, N., Castro, I., Goulart, E.V., Xie, Z., 2023. Influence of wind direction and source location on peak-to-mean concentration ratios in urban environments. J. Wind Eng. Ind. Aerodyn. 232, 105264. http://dx.doi.org/10.1016/j.jweia.2022.105264, URL: https://www.sciencedirect.com/science/article/pii/S0167610522003609.
Minguez, M., Brun, C., Pasquetti, R., Serre, E., 2011. Experimental and high-order LES analysis of the flow in near-wall region of a square cylinder. Int. J. Heat Fluid Flow 32 (3), 558–566.
Mishra, A., Carpentieri, M., Robins, A., Placidi, M., 2024. Experimental study of the turbulent characteristics in the wake of tall building clusters. Flow 4, E15. http://dx.doi.org/10.1017/flo.2024.16, URL: https://www.cambridge.org/core/product/62857E5FFCEA6E9872104CFFF156057A.
Mishra, A., Placidi, M., Carpentieri, M., Robins, A., 2023. Wake characterization of building clusters immersed in deep boundary layers. Bound.-Layer Meteorol. 189, 163–187. http://dx.doi.org/10.1007/s10546-023-00830-0.
Morrison, W., Looschelders, D., Céspedes, J., Claxton, B., Drouin, M.-A., Dupont, J.-C., Faucheux, A., Haeffelin, M., Holst, C.C., Kotthaus, S., et al., 2025. Harmonised boundary layer wind profile dataset from six ground-based doppler wind lidars in a transect across Paris, France. Earth Syst. Sci. Data Discuss. in review, 2025, 1–27.
Nafisifard, M., Jakobsen, J.B., Snæ björnsson, J.T., Sjöholm, M., Mann, J., 2023. Lidar measurements of wake around a bridge deck. J. Wind Eng. Ind. Aerodyn. 240, 105491.
Nandi, T.N., Yeo, D., 2021. Estimation of integral length scales across the neutral atmospheric boundary layer depth: A large eddy simulation study. J. Wind Eng. Ind. Aerodyn. 218, 104715.
Nazarian, N., Lu, J., Lipson, M.J., Hart, M.A., Liu, S., Krayenhoff, E.S., Blunn, L., Martilli, A., 2025. UrbanTALES: A large-eddy simulation dataset for urban canopy layer turbulence and parameterization. Bull. Am. Meteorol. Soc. 106 (12), E2461–E2478.
Nguyen, C.H., Inam, S., Lasagna, D., Xie, Z.-T., 2023. Aerodynamics and wake flow characteristics of a four-cylinder cluster. Flow, Turbul. Combust. 110 (4), 1091–1115.
Olhede, S.C., Walden, A.T., 2002. Generalized morse wavelets. IEEE Trans. Signal Process. 50 (11), 2661–2670.
Park, S.-B., Baik, J.-J., Han, B.-S., 2015. Large-eddy simulation of turbulent flow in a densely built-up urban area. Environ. Fluid Mech. 15 (2), 235–250.
Pascheke, F., Barlow, J.F., Robins, A., 2008. Wind-tunnel modelling of dispersion from a scalar area source in urban-like roughness. Bound.-Layer Meteorol. 126, 103–124.
Perrier, V., Philipovitch, T., Basdevant, C., 1995. Wavelet spectra compared to Fourier spectra. J. Math. Phys. 36 (3), 1506–1519.
Plate, E.J., 1999. Methods of investigating urban wind fields—physical models. Atmos. Environ. 33 (24), 3981–3989. http://dx.doi.org/10.1016/s1352-2310(99)00140-5, URL: https://www.sciencedirect.com/science/article/pii/S1352231099001405.
Raupach, M.R., Shaw, R.H., 1982. Averaging procedures for flow within vegetation canopies. Bound.-Layer Meteorol. 22 (1), 79–90.
Rich, T., Vanderwel, C., 2024. Pollutant Dispersion Around a Single Tall Building. Bound.-Layer Meteorol. 190 (8), 34. http://dx.doi.org/10.1007/s10546-024-00874-w.
Richards, P., Norris, S., 2011. Appropriate boundary conditions for computational wind engineering models revisited. J. Wind Eng. Ind. Aerodyn. 99 (4), 257–266.
Robins, A.G., 1979. The development and structure of simulated neutrally stable atmospheric boundary layers. J. Wind Eng. Ind. Aerodyn. 4, 71–100.
Rodi, W., 1997. Comparison of LES and RANS calculations of the flow around bluff bodies. J. Wind Eng. Ind. Aerodyn. 69, 55–75.
Sessa, V., Xie, Z.-T., Herring, S., 2020. Thermal stratification effects on turbulence and dispersion in internal and external boundary layers. Boundary-Layer Meteorol. 176 (1), 61–83.
Stull, R.B., 2012. An Introduction to Boundary Layer Meteorology. vol. 13, Springer Science & Business Media.
Stull, R., 2016. Practical Meteorology: An Algebra-based Survey of Atmospheric Science. BC Open Textbook Collection, AVP International, University of British Columbia, URL: https://books.google.co.uk/books?id=xP2sDAEACAAJ.
Sun, H., Gao, X., Yang, H., 2020. A review of full-scale wind-field measurements of the wind-turbine wake effect and a measurement of the wake-interaction effect. Renew. Sustain. Energy Rev. 132, 110042.
Theeuwes, N.E., Barlow, J.F., Mannisenaho, A., Hertwig, D., O'Connor, E., Robins, A., 2025. Observations of tall-building wakes using a scanning Doppler lidar. Atmospheric Meas. Tech. 18 (6), 1355–1371.
Torrence, C., Compo, G.P., 1998. A practical guide to wavelet analysis. Bull. Am. Meteorol. Soc. 79 (1), 61–78.
Trias, F., Gorobets, A., Oliva, A., 2015. Turbulent flow around a square cylinder at Reynolds number 22,000: A DNS study. Comput. & Fluids 123, 87–98.
UN, 2014. World urbanization prospects: The 2014 revision, highlights. Department of Economic and Social Affairs. Vol. 32, Population Division, United Nations.
Warren, E., Charlton-Perez, C., Lean, H., Kotthaus, S., Grimmond, S., 2022. Spatial variability of forward modelled attenuated backscatter in clear-sky conditions over a megacity: Implications for observation network design. Q. J. R. Meteorol. Soc. 148 (744), 1168–1183.
Wong, M.S., Nichol, J.E., To, P.H., Wang, J., 2010. A simple method for designation of urban ventilation corridors and its application to urban heat island analysis. Build. Environ. 45 (8), 1880–1889.
Wood, C.R., Arnold, S.J., Balogun, A.A., Barlow, J.F., Belcher, S.E., Britter, R.E., Cheng, H., Dobre, A., Lingard, J.J., Martin, D., et al., 2009. Dispersion experiments in central London: the 2007 DAPPLE project. Bull. Am. Meteorol. Soc. 90 (7), 955–970.
Wood, C., Lacser, A., Barlow, J.F., Padhra, A., Belcher, S.E., Nemitz, E., Helfter, C., Famulari, D., Grimmond, C., 2010. Turbulent flow at 190 m height above London during 2006–2008: a climatology and the applicability of similarity theory. Bound.-Layer Meteorol. 137, 77–96.
Xie, Z.-T., 2011. Modelling street-scale flow and dispersion in realistic winds—towards coupling with mesoscale meteorological models. Bound.-Layer Meteorol. 141, 53–75.
Xie, Z.-T., Castro, I.P., 2006. LES and RANS for turbulent flow over arrays of wall-mounted obstacles. Flow Turbul Combust 76 (3), 291.
Xie, Z.-T., Castro, I.P., 2008. Efficient generation of inflow conditions for large eddy simulation of street-scale flows. Flow Turbul Combust 81 (3), 449–470.
Xie, Z.-T., Castro, I.P., 2009. Large-eddy simulation for flow and dispersion in urban streets. Atmos. Environ. 43 (13), 2174–2185.
Xie, Z.-T., Coceal, O., Castro, I.P., 2008. Large-eddy simulation of flows over random urban-like obstacles. Bound.-Layer Meteorol. 129 (1), 1–23.
Xie, Z.-T., Fuka, V., 2018. A note on spatial averaging and shear stresses within urban canopies. Boundary-Layer Meteorol 167 (1), 171–179.
Xie, Z.-T., Voke, P.R., Hayden, P., Robins, A.G., 2004. Large-eddy simulation of turbulent flow over a rough surface. Bound.-Layer Meteorol. 111, 417–440.